

Crystallographic, Energy Gap, Photoluminescence and Photo-Catalytic Investigation of Cu Doped $\text{Cd}_{0.9}\text{Zn}_{0.1}\text{S}$ Nanostructures by Co-Precipitation Method

P. Raju (✉ praju12345@yahoo.com)

Manonmaniam Sundaranar University <https://orcid.org/0000-0002-0834-0099>

Joseph Prince Jesuraj

University College of Engineering, Bharathidasan Institute of Technology Campus, Anna University

S. Muthukumaran

Government Arts College

Research Article

Keywords: Zn, Cu doped CdS, Crystallite size, Energy gap, Photoluminescence, Photo-catalytic activity

Posted Date: April 29th, 2021

DOI: <https://doi.org/10.21203/rs.3.rs-457743/v1>

License:   This work is licensed under a Creative Commons Attribution 4.0 International License.

[Read Full License](#)

Abstract

The controlled synthesis of $\text{Cd}_{0.9}\text{Zn}_{0.1}\text{S}$, $\text{Cd}_{0.89}\text{Zn}_{0.1}\text{Cu}_{0.01}\text{S}$ and $\text{Cd}_{0.87}\text{Zn}_{0.1}\text{Cu}_{0.03}\text{S}$ nanostructures by simple chemical co-precipitation technique was reported. The XRD investigation confirmed the basic CdS cubic structure on Zn-doped CdS and also Zn, Cu dual doped CdS with no secondary/impurity related phases. No modification in cubic structure was detected during the addition of Zn/Cu into CdS. The reduction of crystallite size from 63 Å to 40 Å and the changes in lattice parameter confirmed the incorporation of Cu into $\text{Cd}_{0.9}\text{Zn}_{0.1}\text{S}$ and generation of Cu related defects. The shift of absorption edge along upper wavelength region and elevated absorption intensity by Cu doping can be accredited to the collective consequence of quantization and the generation of defect associated states. The enhanced optical absorbance and the reduced energy gap recommended that $\text{Cd}_{0.87}\text{Zn}_{0.1}\text{Cu}_{0.03}\text{S}$ nanostructure is useful to enhance the efficiency of opto-electronic devices. The presence of Cd-S / Zn-Cd-S / Zn/Cu-Cd-S chemical bonding were confirmed by Fourier transform infrared investigation. The elevated green emissions by Cu incorporation was explained by decrease of crystallite size and creation of more defects. Zn, Cu dual doped CdS nanostructures are recognized as the possible and also efficient photo-catalyst for the removal dyes like methylene blue. The enhanced photo-catalytic behaviour of Zn, Cu dual doped CdS is the collective consequences of high density electron-hole pairs creation, enhanced absorbance in the visible wavelength, surface area enhancement, reduced energy gap and the formation of novel defect associated states. The stability measurement signified that Cu doped $\text{Cd}_{0.9}\text{Zn}_{0.1}\text{S}$ exhibits superior dye removal ability and better stability even after 6 repetitive runs with limited photo-corrosion.

1. Introduction

Semiconducting nanostructured materials play an important role in the latest research technology [1]. The properties of these nanostructured materials change abruptly during the reduction of crystallite size into lower levels. The nano-sized II-VI group semiconducting materials have drawn considerable curiosity in the latest years by their distinctive properties which promotes them for a novel applications in different fields like solar cells, LEDs, photo-catalytic applications [2–5]. The broad band gap exhibited in semiconducting nanomaterials is really significant one and this property makes it possible to produce light emitting diodes and laser devices for emission in the spectrum of the visible wavelengths [6]. The nanostructured semiconducting metal oxides like ZnO, CdO and metal sulfides like ZnS, CdS are attracted considerable attention as light emission substances because of their size and energy gap tuning [7, 8].

In the modern era, cadmium sulfide (CdS), the most significant II-VI semiconducting materials drawn a great attention by its probable applications in various fields like display panels [9], luminescence activators [10] transistors [11] and photo-catalytic [12, 13]. CdS is a wide and direct band gap semiconducting materials with energy gap around ≈ 2.42 eV [14] at room temperature and hence it can execute as an outstanding photo-catalytic material responsive to visible-light irradiation [15, 16]. Since, CdS is a prominent luminescence activator it finds various applications in photo-conductive, electroluminescent and photo-luminescent devices [17–20]. Moreover, CdS exhibits elevated refractive

index [21], a little exciton Bohr radius about ~ 2.5 nm, tremendous transport character and better chemical as well as thermal stability [22].

The three possible structures of CdS are cubic, hexagonal and rock salt [23]. Compared with other phases, the hexagonal phase is thermodynamically stable at room temperature. Rock phase exists at high pressure and cubic phase of CdS appears at 1 atmosphere of very small and nano-sized particles [17]. Cubic structure of CdS is transformed into hexagonal structure by the influence of annealing temperature owing to the generation of defects and the defect associated faults within Cd-S lattice [17]. Banerjee et al. [24] reported that CdS nanostructures existing at mixer of cubic as well as hexagonal structures around 4 to 5 nm crystallite size and the CdS survived with pure cubic structure below the 4–5 nm size and appeared with hexagonal structure above said crystallite size. In addition, the transformation of phases between cubic and hexagonal can be done by the addition of appropriate amount of dopants into Cd-S lattice [25].

The doping of elements into CdS nanostructures is one of the most excellent procedures for the adjustment of electrical or thermal conductivity and also the band gap. Particularly, the doping of transition metals (TMs) introduces the different deep levels inside the energy gap which can adjust not only the optical nature of the materials and also modify the electro-chemical and electrical characteristics and hence induces various practical applications in different modern fields of technology [26]. Different TM ions like Ga [27], Sn [28], B [29], Cu [30], In [31], and Zn [32, 33], have been doped into CdS in order to improve its optical, magnetic, photoluminescence and electrical characteristics.

Within the different doping elements, Zn is considered as the first dopant to alter the size, optical, electrical, magnetic structural, photoluminescence and photo-catalytic characteristics of CdS lattice by replacing Cd^{2+} ions and to create Cd-Zn-S nanostructures [34]. Zn can easily replace Cd^{2+} ions in CdS because of the ionic radius of Zn^{2+} (~ 0.74 nm) is close to that of Cd^{2+} ions (~ 0.97 nm) [34]. The substitution of Zn^{2+} increases the energy gap of CdS with no alteration in its crystal structure [35]. The enhanced energy gap is essential for the solar cell which creates the better transparency in visible wavelength and diminish in the window absorption losses and hence enhances the short circuit current [36]. Due to the enhanced energy gap and reduced crystallite size by Zn incorporation in CdS improves the photo-catalytic behaviour of Zn-CdS composite material with better photo-catalytic stability and higher surface to volume ratio [37] which is crucial to generate the new and novel materials. Based on the detailed structural, optical and photoluminescence investigations of Zn doped CdS [38], Zn doping concentration is limited to 10% ($\text{Cd}_{0.9}\text{Zn}_{0.1}\text{S}$).

For the further enhancement in the structure, electrical and photoluminescence characteristics of $\text{Cd}_{0.9}\text{Zn}_{0.1}\text{S}$ without generating an additional phases, Cu is chosen as the second doping element. Cu ions performs as an acceptors in CdS which alter the electrical resistivity, energy gap, photo-electrical characteristics and also transform the semiconducting CdS from n to p type material [39]. The addition of Cu into CdS enhances the photo-sensitivity of the materials and also transforms it to p-type material [40, 41]. The reduced energy gap of CdS by Cu doping may be due to the surface morphology, structural

changes and the incorporation of Cu ions which can restore either interstitial or substitutional Cd ions in the Cd-S lattice [42]. The visible light response of Zn-doped CdS system was enhanced by the Cu contribution in Cd-Zn-S system [43]. Singh et al. [44] reported that Ag⁺ and Cu²⁺ doping of CdS enhanced the optical, distortion in crystal structure, and better photocatalytic properties and they described that the addition of Ag⁺ and Cu²⁺ in CdS induced the narrowing of band edge potentials and distortion in the crystal. The ionic radius of Zn²⁺, Cd²⁺ and Cu²⁺ are found to be 0.74 Å, 0.97 Å and 0.72 Å, respectively. As a result, Cu can easily replaced either as substitutional or interstitial in position of Cd²⁺ [45]. When Cu is increased to higher levels, Cu related impurity or secondary phases may induced in the host lattice [46, 47]. Therefore, to avoid the unwanted secondary phases, the doping percentage of Cu is limited to 3% in the present investigations.

Though the comprehensive investigation on crystallographic, structural and optical properties of Zn / Cu doped CdS have been carried out [34–43, 45–47], the detailed analysis of Zn and Cu dual doped CdS nano-system is still scanty. Therefore, the present investigation focused on the preparation of Cd_{0.9}Zn_{0.1}S and Cu = 1 % and 3% doped Cd_{0.9}Zn_{0.1}S using co-precipitation route. The structural, FTIR, optical, photoluminescence and photo-catalytic assessments on Zn-doped CdS and Zn, Cu dual doped CdS nanostructures were thoroughly explored and the attained outcomes are interpreted.

2. Experimental Details

2.1. Synthesis of Cu doped Cd_{0.9}Zn_{0.1}S (Cu = 0, 1 and 3%) nanostructures

Zn and Cu simultaneously doped CdS nanostructures were synthesized by co-precipitation route. The co-precipitation route is selected in the present work because any one can change the dopant as well as doping levels easily, synthesized samples exhibit better quality and controlled doping [31].

Cadmium acetate dihydrate (Cd(CH₃COOH)₂·2H₂O), zinc acetate dihydrate [Zn(CH₃COO)₂·2H₂O], copper acetate dihydrate (Cu(CH₃COOH)₂·2H₂O), and sodium sulfide (Na₂S) have been used as the precursors for the preparation of Zn and Cu simultaneously doped CdS without additional purification. All entire chemical engaged in this work were analytical grade (AR) and high purity (>99% purity). The chemicals, Cd(CH₃COOH)₂·2H₂O, Cu(CH₃COOH)₂·2H₂O, Zn(CH₃COO)₂·2H₂O, and Na₂S were procured from Merck chemical company and they are the source of Cd²⁺, Cu²⁺, Zn²⁺ and S²⁻ ions, respectively. The procedure to the synthesize the above material is as reported in the our previous paper [38]. The flowchart and the synthesis procedure of Zn and Ni simultaneously doped CdS nanostructures is as shown in Fig. 1.

The pH value is retained as 8.5 by the adding of aqueous ammonia solution. Nearly yellow color output was filtered and rinsed a number of times by high purity distilled water and ethanol to remove the pollution. The collected precipitates were dried using an oven at 100°C for 8 h. The color of Cd_{0.9}Zn_{0.1}S

nano-powder is found to be yellow that is altered to light brown for Cu = 1% and dark brown for Cu = 3% doped $\text{Cd}_{0.9}\text{Zn}_{0.1}\text{S}$ as shown in Fig. 2.

2.2. Characterization techniques

The diffracted patterns of the prepared samples were carried out using RigakuC/max-2500 diffractometer with Cu K α radiation from $2\theta = 20^\circ$ to 60° . The surface morphology of the synthesized samples was studied using scanning electron microscope (SEM, JEOLJSM 6390, Japan). The presence of constitutional elements like Cd, Cu, Zn and S were confirmed by energy dispersive X-ray spectrometer on K and L lines.

The optical absorption spectra have been obtained using UV–Visible spectrometer (Model: lambda 35, Make: Perkin Elmer) from 300 to 600 nm at ambient temperature with necessary software. The presence of chemical bonding was studied by FTIR spectrometer (Model: Perkin Elmer, Make: Spectrum RX I) from 400 to 4000 cm^{-1} . The photoluminescence (PL) spectra have been carried out between the wavelength ranging from 350 nm to 590 nm under the excitation of Xenon lamp laser with 320 nm line using a fluorescence spectrophotometer (F-2500, Hitachi) at room temperature.

Photocatalytic activities of the synthesized samples were carried out on methylene blue (MB) using UV–Vis spectrophotometer. MB stock solution (2 mmol) was prepared in de-ionized (DI) water. 50 mL of prepared MB solution (reactant) was taken into a 100 mL beaker and kept on the magnetic stirrer. Subsequently, 10 mg of the catalyst (synthesized samples) was added into the reactant and irradiations were carried out under UV light (wavelength 360 nm, distance 80 mm, power 80 W) under mild stirring. After UV irradiation, 1 mL of the solution was taken out from the solution at certain time intervals (0 to 3h) and centrifuged to get the upper clear solution.

3. Result And Discussions

3.1. X-ray diffraction (XRD) – structural studies

In order to investigate the structure, size, lattice parameters and micro-strain of $\text{Cd}_{0.9}\text{Zn}_{0.1}\text{S}$, $\text{Cd}_{0.89}\text{Zn}_{0.1}\text{Cu}_{0.01}\text{S}$ and $\text{Cd}_{0.87}\text{Zn}_{0.1}\text{Cu}_{0.03}\text{S}$ nanostructures, the XRD spectra were recorded between 20° and 60° and presented in Fig. 3. All the three recorded diffraction peaks were well broaden which indicates the nano-crystalline nature with smaller crystallite size of the synthesized samples [48]. Among the three different peaks, the high intensity peak corresponding to (111) orientation is chosen to analyze the crystallite size and micro-strain. The XRD peaks of $\text{Cd}_{0.9}\text{Zn}_{0.1}\text{S}$ nanostructure are well matched with JCPDS file of CdS (JCPDS card No. 89-0440). The observed cubic structure of CdS throughout the samples is in good agreement with the earlier studies [49, 50]. Dutkova and their co-workers [51] also reported that hexagonal structure of CdS was changed to cubic structure at Zn = 10% ($\text{Cd}_{0.9}\text{Zn}_{0.1}\text{S}$).

No additional XRD peaks noticed from Fig. 3 that represents the absence of metal/sulfide/oxide phases of Cd, Zn/Cu or other impurity related secondary phases in the Cd-Zn-Cu-S lattice. Moreover, the present XRD pattern verifies the phase singularity as well as the formation of Cd-Cu-Zn-S alloy at nano-scale. The detected more or less identical diffractions along the entire Cu doped nano-system proves that the cubic structure of the present samples remain un-changed by the addition of Cu ions in Cd-Zn-S lattice.

Fig. 4 reveals the variation of peak intensity as well as peak position through (111) orientation for different Cu concentrations from 0 % to 3%. The continuous decrease of XRD peak intensity reflects the diminishing crystallite size and signifies the deterioration of crystalline quality. The similar decrease of peak intensity was reported in CdS with addition of Cu levels up to 5% by Muruganandam et. al [52]. In the case of peak position change, it falls down moderately at Cu = 1% and increases slightly during Cu = 3% addition. Both the decrease of peak intensity as well as the modification in peak position as seen in Fig. 4 indicates the substitution of Cu into Cd-Zn-S lattice.

Table 1 represents the variation in peak position (2θ value), FWHM value, d-value, cell parameter 'a', crystallite size (D) and micro-strain (ϵ) of $\text{Cd}_{0.9}\text{Zn}_{0.1}\text{S}$, $\text{Cd}_{0.89}\text{Zn}_{0.1}\text{Cu}_{0.01}\text{S}$ and $\text{Cd}_{0.87}\text{Zn}_{0.1}\text{Cu}_{0.03}\text{S}$ nanostructures. The crystallite size of the synthesized samples is calculated with the help of Scherrer relation [53], $0.9 \lambda / b \cos \theta$, here $\lambda \approx 1.5406 \text{ \AA}$. The micro-strain (ϵ) of the synthesized samples is analyzed using the relation [54], $b \cos \theta / 4$. The addition of Cu generates the additional defect states associated with Cu impurity and also stimulates the structural disorder in the Cd-Zn-S lattice [55] which are responsible for the adjustment in peak intensity as well as the peak position.

The crystallite size of $\text{Cd}_{0.9}\text{Zn}_{0.1}\text{S}$ nanostructure ($D \sim 63 \text{ \AA}$) is rapidly decreased to 46 \AA by doping Cu = 1% and reduced to 40 \AA for Cu = 3% addition. The decrease of crystallite size is due to the difference between the ionic radii of Cu^+ (0.96 \AA), Cu^{2+} (0.72 \AA) and Cd^{2+} (0.97 \AA) ions, where Cu^+ and Cu^{2+} are smaller than that of Cd^{2+} [56]. The substitution of Cd ions by Cu ions influence the lattice parameter 'a' and the inter-planar distance 'd' which lead the decrease of volume of the unit cell and hence the crystal size is also reduced. The increase of micro-strain by Cu addition as shown in Table 1 is also accountable for the widening of diffraction peaks [57, 58]. The comparable raise of lattice parameters and the reduction of size was reported by Woltersdorf et al. [59]. Moreover, the addition of Cu^{2+} induces the lattice distortion in Cd-Zn-S matrix which enhances the lattice constant of Cu-doped $\text{Cd}_{0.9}\text{Zn}_{0.1}\text{S}$ than undoped $\text{Cd}_{0.9}\text{Zn}_{0.1}\text{S}$ nanostructures [60].

3.2. SEM - Surface morphology

SEM is used to analyze the surface structure, size and shape of the particles / grains and also growth mechanism. Fig. 5 shows the SEM images of $\text{Cd}_{0.9}\text{Zn}_{0.1}\text{S}$, $\text{Cd}_{0.89}\text{Zn}_{0.1}\text{Cu}_{0.01}\text{S}$ and $\text{Cd}_{0.87}\text{Zn}_{0.1}\text{Cu}_{0.03}\text{S}$ nanostructures. Fig. 5a shows the morphology of $\text{Cd}_{0.9}\text{Zn}_{0.1}\text{S}$ nanostructure. The observed grain size of the system is within the nano-scale levels. The SEM image of $\text{Cd}_{0.9}\text{Zn}_{0.1}\text{S}$

nanostructures shows the irregular distribution of particles / grains within the agglomerated cluster throughout the surface with fine grained structure. The noticed gains are almost spherical in shape.

Fig. 5b represents the surface structure of $\text{Cd}_{0.89}\text{Zn}_{0.1}\text{Cu}_{0.01}\text{S}$ nanostructures. The surface became more dense than $\text{Cd}_{0.9}\text{Zn}_{0.1}\text{S}$ and the grain size is reduced by Cu doping (Cu = 1%). The grains are combined together and form a flower like structure. The reduced size as seen in Fig. 5b is owing to the elevated micro-strain, and the lattice imperfection and defects stimulated by Cu doping. Fig. 5c shows the surface structure of $\text{Cd}_{0.87}\text{Zn}_{0.1}\text{Cu}_{0.03}\text{S}$ nanostructures. The island growth pattern is noticed from Fig. 5c which could be owing to fast nucleation rate and rapid crystal growth of Cd-Fe-S and also existence of excess free cadmium metal ions. Among the combination of plate-like as well as spherical-like grain structure, plate-like structure is dominated at Cu = 3% doping.

3.3. EDX- Compositional analysis

EDX analysis is used to verify the occurrence of Cd, S, Zn and Cu as the basic constitutional components. The characteristic EDX spectra of $\text{Cd}_{0.9}\text{Zn}_{0.1}\text{S}$, $\text{Cd}_{0.89}\text{Zn}_{0.1}\text{Cu}_{0.01}\text{S}$ and $\text{Cd}_{0.87}\text{Zn}_{0.1}\text{Cu}_{0.03}\text{S}$ nanostructures are shown in Fig. 6a-c, respectively. The quantitative atomic % of the fundamental elements such as Cd, S, Zn and Cu existing in the synthesized samples using EDX analysis is presented in Table 2. The noticed well defined peaks related to the elements Cd, S, Zn, and Cu confirmed the stoichiometry of the samples at the finally prepared composite. The higher atomic percentage of Cd (more than 52%) than other elements reveals the Cd rich phase throughout the samples as reported in the literature [61].

Absence of additional peaks matching to the elements other than Cd, S, Zn, and Cu indicates the phase purity of the samples. The atomic percentage of Zn remains almost constant but Cu level increases gradually which express that Cu is properly inserted into Cd-Zn-S lattice. Moreover, the Cu / (Cd+Zn+Cu) ratios are found to be 0.98 and 3.2% for $\text{Cd}_{0.89}\text{Zn}_{0.1}\text{Cu}_{0.01}\text{S}$ and $\text{Cd}_{0.87}\text{Zn}_{0.1}\text{Cu}_{0.03}\text{S}$ nanostructures, respectively. The atomic fraction of Zn and Cu are almost equal to their nominal stoichiometry within the experimental error.

3.4. Optical absorption and transmittance studies

Optical characteristics such as optical absorption along visible wavelength, transmittance and the wide range of energy gap plays a considerable role in the selection of materials for the appropriate opto-electronic device applications. Fig. 7 displays the optical absorption of $\text{Cd}_{0.9}\text{Zn}_{0.1}\text{S}$, $\text{Cd}_{0.89}\text{Zn}_{0.1}\text{Cu}_{0.01}\text{S}$ and $\text{Cd}_{0.87}\text{Zn}_{0.1}\text{Cu}_{0.03}\text{S}$ nanostructures at ambient temperature from 300 nm to 600 nm.

$\text{Cd}_{0.9}\text{Zn}_{0.1}\text{S}$ nanostructure exhibits a strong absorption below 330 nm and above this wavelength the absorption falls down abruptly which indicates the energy gap of the substance. The low level Cu addition (Cu = 1%) into $\text{Cd}_{0.9}\text{Zn}_{0.1}\text{S}$ moves the absorption edge slightly towards the visible wavelength area (red shift). The noticed red shift becomes stronger during the further addition of Cu (Cu = 3%). The

prominent absorption below ≈ 360 nm is initiated from the conversion of electrons from valence level to the conduction level which signifies the energy gap of the materials [62]. In addition to the absorption edge shift towards lower energy region, the absorption intensity is also increased by Cu doping. Moreover, no extra absorption peaks noticed from Fig. 7 ruled out presence of impurity or secondary phase generation in the Cd-Zn-Cu-S alloy. The continuous red shift of absorption edge is also supported by the occurrence of d-d transition between $\text{Cu}^{2+}/\text{Zn}^{2+}/\text{Cd}^{2+}$ ions [63,64]. The shift of absorption edge along upper wavelength region and elevated absorption intensity by Cu doping can be accredited to the collective consequence of quantization and the generation of defect associated states.

The characteristic transmittance spectra of $\text{Cd}_{0.9}\text{Zn}_{0.1}\text{S}$, $\text{Cd}_{0.89}\text{Zn}_{0.1}\text{Cu}_{0.01}\text{S}$ and $\text{Cd}_{0.87}\text{Zn}_{0.1}\text{Cu}_{0.03}\text{S}$ nanostructures at ambient temperature from 300 nm to 600 nm is shown in Fig. 8. All the three samples possess high transmittance after 350 nm i.e., in the visible wavelength region followed by a steep increase around UV wavelengths. un-doped $\text{Cd}_{0.9}\text{Zn}_{0.1}\text{S}$ nanostructure acquires a high transmittance in the visible region which is decreased gradually by Cu doping. The present decrease in transmittance may be due to the reduction of size and hence more light scattering by Cu doping [65,66]. The one more reason to diminish the transmittance is the increase of packing density which exhibits an inverse correlation with transmittance [67]. In addition, the shift of transmittance edge along lower energy side (red shift) by Cu doping denotes the creation of new states under the conduction band which indicates the diminution of energy gap.

3.5. Energy gap calculation

The energy gap of $\text{Cd}_{0.9}\text{Zn}_{0.1}\text{S}$, $\text{Cd}_{0.89}\text{Zn}_{0.1}\text{Cu}_{0.01}\text{S}$ and $\text{Cd}_{0.87}\text{Zn}_{0.1}\text{Cu}_{0.03}\text{S}$ nanostructures is estimated [68] by deriving the straight line to the plot of $(ah\nu)^2$ versus the energy $(h\nu)$. Fig. 9 illustrates the variation in the energy gap of Zn-doped CdS and Cu, Zn dual doped CdS nanostructures which is obtained by the graph between $(ah\nu)^2$ and $h\nu$. The energy gap of the synthesized materials is found between 3.69 eV ($\text{Cd}_{0.87}\text{Zn}_{0.1}\text{Cu}_{0.03}\text{S}$) and 3.99 eV ($\text{Cd}_{0.9}\text{Zn}_{0.1}\text{S}$) which is superior than the CdS (2.42 eV) [69]. The obtained higher energy gap is owing to the smaller crystallite size (40-63 Å) which possesses the higher surface to volume ratio and hence the lower spatial dimension [70].

The derived energy gap of $\text{Cd}_{0.9}\text{Zn}_{0.1}\text{S}$ from Fig. 9 is 3.99 eV which is shifted to lower value as 3.93 eV by Cu = 1% doping and further decreased to 3.69 eV for Cu = 3% doping. The diminishing energy gap by Cu doping suggests the proper substitution of Cu into $\text{Cd}_{0.9}\text{Zn}_{0.1}\text{S}$ nanostructure. A typical energy level diagram to describe the red shift of energy gap by Cu doping is presented as shown in Fig. 10. The present shrinkage of energy gap by Cu incorporation can be associated to the development of Cu related impurity levels related to Cu acceptor level [71] below the conduction band as shown in Fig. 10. A slight decrease of energy gap was reported in Cu doped CdS synthesized by mechanical alloying [72]. Kato et al. [73] proposed the decline of energy gap by the presence of Cu based acceptor levels above valence band. Aksu et al. [74] reported the decrease of energy gap from 2.42 eV to 2.36 eV in vacuum evaporated CdS structure by Mn addition. Moreover, Mariappan et al. [49] reported the optical transmittance below \sim

50% and also the shrinkage of energy gap from 2.5 to 2.2 eV by Cu added CdS thin films prepared using CBD method. Therefore, it is suggested that TM doping into Cd-Zn-S nanostructure is an efficient approach to reduce its optical energy gap.

Fig. 11 presents the modification of crystallite size as well as energy gap for different Cu concentration levels from 0 to 3%. Normally, the crystallite size and band gap of the substance are conflicting to each other. Both the energy gap and crystallite size falls down continuously with increase of Cu levels as displayed in Fig. 11. The present diminishing energy gap occurred by the energy transport process between CdS excited states and 3d levels of Cu^{2+} . Moreover, the crystallite size is superior than the excitonic Bohr radius and hence the size effect is insignificant to explain the band gap alteration. The generation of more Cu related defects and the creation of structural deformations [75,76] are responsible for the size reduction and the decrease of energy gap. The comparable crystallite size alteration and the consequent red shift in band gap were noticed in Co^{2+} doped ZnS films using dip coating technique [77] and spin coating technique [78] in the previous research.

3.6. Fourier transform infrared (FTIR) studies

With the intention of confirming the existence of constitutional elements such as Cd, S, Zn, and Cu and chemical bonding between Cd and Zn/Cu-S, FTIR spectra have been carried out between 400 to 4000 cm^{-1} at ambient temperature. Fig. 12 illustrates the FTIR spectra of $\text{Cd}_{0.9}\text{Zn}_{0.1}\text{S}$, $\text{Cd}_{0.89}\text{Zn}_{0.1}\text{Cu}_{0.01}\text{S}$ and $\text{Cd}_{0.87}\text{Zn}_{0.1}\text{Cu}_{0.03}\text{S}$ nanostructures evaluated using KBr pellet method. IR peaks and their assignments of $\text{Cd}_{0.9-x}\text{Zn}_{0.1}\text{Cu}_x\text{S}$ ($x = 0, 0.01$ and 0.03) nanostructures at room temperature obtained from FTIR spectra are presented as Table 3. The broad absorption bands around 3396-3493 cm^{-1} signified the polymeric O-H stretching vibrations [79], which are showing the existence of H_2O molecules at the surface of the nanomaterials. The strong bands arising between 1592-1631 cm^{-1} associated to the bending vibration of H-O-H molecules [80] in $\text{Zn}^{2+}/\text{Cu}^{2+} : \text{Cd-S}$ lattice.

The feeble absorption bands from 793-861 cm^{-1} were illustrated the structural deformation and micro-structure formation related with defect states created by Cu^{2+} ions through Cd-Zn-S lattice. The characteristic peaks around 428-432 cm^{-1} and 683-671 cm^{-1} represented the $\text{Zn}^{2+}/\text{Cu}^{2+} : \text{Cd-S}$ lattice vibrations [81, 82]. The alteration in intensity of characteristic bands between 400-700 cm^{-1} and peak shift from 671 cm^{-1} to 685 cm^{-1} by Cu addition not only signify the size reduction and also convey the substitution of Cu^{2+} into Cd-Zn-S lattice network.

3.7. Photoluminescence (PL) studies

Fig. 13 presents the PL spectra of $\text{Cd}_{0.9}\text{Zn}_{0.1}\text{S}$, $\text{Cd}_{0.89}\text{Zn}_{0.1}\text{Cu}_{0.01}\text{S}$ and $\text{Cd}_{0.87}\text{Zn}_{0.1}\text{Cu}_{0.03}\text{S}$ nanostructures between 350 nm and 590 nm. PL spectra of Zn-doped CdS ($\text{Cd}_{0.9}\text{Zn}_{0.1}\text{S}$) includes two broad visible PL emissions. The first prominent band centered at 386 nm ($E_g \sim 3.22$ eV) corresponding to bluish-violet (BV) emission and the second broad band with lower intensity located at 541 nm ($E_g \sim 2.30$

eV) connected to the green emission (GE) bands. The two main reasons behind origin of photoluminescence emissions are the transition of charges between conduction band to valence band i.e., recombination of two opposite charges, electron and holes in semiconductors and other one is from the transition of charges between the surface defect states i.e., the recombination of charges through the defect states [83]. Fig. 14 illustrates the energy level diagram to explore the two visible emissions such as BV and GE bands. The noticed strong BV band around ~ 386 nm is initiated from the presence of the interstitials of Cd^{2+} (I_{Cd}). The weak GE band observed in $\text{Cd}_{0.9}\text{Zn}_{0.1}\text{S}$ around ~ 541 nm is originated from the recombination of shallow electrons trapped within a sulfur vacancy and hole pair from surface/defect related site to the valence band [84-86]. The similar GE band was reported by Arora et al. [87] around ≈ 530 nm in Mn^{2+} doped CdS nanostructures.

The PL intensity of BV emission band decreases at the same time the intensity of GE band increases by Cu incorporation. The diminishing BV band by Cu addition may be due to the decrease of Cd^{2+} interstitials which was confirmed by EDX spectra (Fig. 6). Generally, the PL emission at high energy is related with high energy recombination centers connected with intrinsic defects or Cu induced defect states [60]. The addition of Cu generates more defects and surface states. The present GE band around 541-548 nm can be accredited to transition among the impurity levels within the energy gap i.e., between the localized surface states [88]. In addition to the emission intensity changes, the peak position is also shifted to higher wavelength side (red-shift) with the rise of Cu doping levels. The similar red shift was reported by Panda et al. [89] in Cu-doped CdS thin films. The tuning of energy gap and also the PL emissions suggest the Cu-doped Cd-Zn-S materials for the high efficient opto-electronic applications.

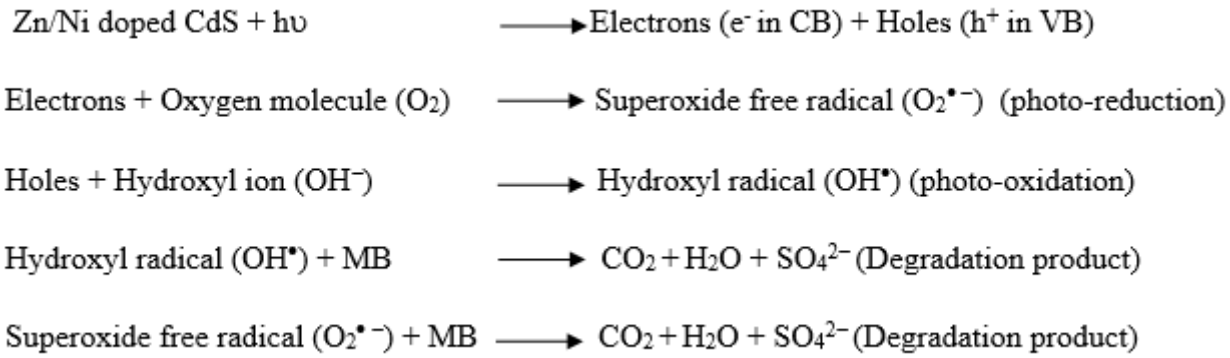
3.8. Photocatalytic activity

Methylene blue (MB) is the solid and odorless chemical which is the main water contaminants discharging from the textile factories. It exhibits blue colour during the dissolution with water at room temperature and also dangerous for the environment. In the present investigation, Zn doped CdS and Zn, Cu dual doped CdS are employed as efficient photo-catalyst to remove the poisonous MB from textile wastage. The decreasing energy gap and the elevated optical absorption of Cu added $\text{Cd}_{0.9}\text{Zn}_{0.1}\text{S}$ nanostructure is probable to perform an imperative role to elevate the efficiency of dye removal capacity. Here, the UV radiation is employed as the light source and the irradiation time is between 0-180 minutes in the interval of 30 minutes. The maximum wavelength of MB is shown between 620-665 nm from the optical absorption measurements [90].

The graphical illustration to express the probable photo-degradation of MB solution using Zn, Cu dual doped CdS as catalyst with different UV radiation exposure times is presented in Fig. 15. During the UV radiation is exposed on Zn, Cu dual doped CdS samples, more number of electrons are liberated into conduction band and hence, plenty of electron-hole pairs available. Generally, the liberation of electron-hole pairs enhances the photo-catalytic dye removal efficiency of the materials [91]. When Cu is incorporated into Cd-Zn-S lattice the energy gap gets diminished which enables the collection of more photons to penetrate the energy gap and increases the electron-hole pairs [56, 92]. The addition of Cu and

Zn into CdS re-structure the energy gap and generate more defect states which enhance the dye removal capacity under UV light exposure [93].

It is renowned that the hydroxyl radicals (OH^\bullet) and superoxide free radicals ($\text{O}_2^{\bullet -}$) in the Zn and Cu doped CdS are the potential oxidizing agents in the degrading MB dyes [94]. The suggested photo-reaction mechanism can be demonstrated as follows:



The final products after the photo-degradation reaction and the dis-integration of MB dye are H_2O , CO_2 , and SO_4^{2-} . Fig. 16 represents the absorption spectra of MB solution with $\text{Cd}_{0.9}\text{Zn}_{0.1}\text{S}$ and $\text{Cd}_{0.87}\text{Zn}_{0.1}\text{Cu}_{0.03}\text{S}$ samples as a photo-catalyst for various exposure times between 0 to 180 minutes. Here, the pure MB solution with no catalyst is taken as a control.

In all two cases, the absorption decreases continuously with the increase of light exposure time. Compared with $\text{Cd}_{0.9}\text{Zn}_{0.1}\text{S}$, Cu doped $\text{Cd}_{0.9}\text{Zn}_{0.1}\text{S}$ sample exhibits better optical absorption reduction capacity.

In order to obtain the better understanding related to the dis-integration of MB, a plot is drawn between the concentration ratio (C_t/C_0) of MB and light exposure time from 0 to 180 minutes as illustrated in Fig. 17a. The variation of dye removal capacity of pure MB dye, $\text{Cd}_{0.9}\text{Zn}_{0.1}\text{S}$ and $\text{Cd}_{0.87}\text{Zn}_{0.1}\text{Cu}_{0.03}\text{S}$ samples as a function of light exposure time is presented in Fig. 17b. The degradation efficiency (η) can be obtained from the relation [95], $\eta (\%) = [(C_0 - C_t) / C_0] \times 100 = [(A_0 - A_t) / A_0] \times 100$ where, C_0 and C_t are concentration of the dye at the light exposure time, '0' and 't' minutes, respectively, and A_0 and A_t are the its equivalent absorption.

Dye removal efficiency is increased with the light exposure time as well as the by the Cu doping. The maximum degradation efficiency of $\text{Cd}_{0.9}\text{Zn}_{0.1}\text{S}$ and Cu doped $\text{Cd}_{0.9}\text{Zn}_{0.1}\text{S}$ are 84 and 98%, respectively at 180 minutes. Generally, the dye removing capacity depends on the crystallite / grain size, micro-structural changes, energy gap and optical absorption intensity [96]. It is easily understood from Fig. 17 that the photo-catalytic activity is enhanced by Cu doping. The noticed higher photo-catalytic behaviour at Cu doped $\text{Cd}_{0.9}\text{Zn}_{0.1}\text{S}$ is due to the reduced crystallite size, elevated surface to volume ratio, increase the range and absorption intensity, enhanced utilization rate and capture of the incident light

which ultimately improving the degradation efficiency. The reduced size enhances the active sites which made more interaction of dye molecules with the surface of the nanostructures and ensure the better photo-catalytic behaviour [97]. Therefore, it is suggested that the improved photo-catalytic behaviour at Cu doped sample is the collective results of high density electron-hole pairs creation, enhanced absorbance in the visible wavelength, surface area enhancement, reduced energy gap and the formation of novel defect associated states [98].

3.9. Stability and re-usability studies

As a helpful photo-catalyst, the stability and the re-usability of the substance are the significant factors for its practical usage in industrial applications. Fig. 18 illustrates the re-usability of Cu doped $\text{Cd}_{0.9}\text{Zn}_{0.1}\text{S}$ catalysts for MO dye removal efficiency at six runs of re-cycling process under UV radiation with light exposure time of 180 minutes. For every cycle, the sample was cleaned repeatedly by de-ionized water and dehydrated using oven at 80°C . The cleaned sample was employed again for the photo-catalytic degradation measurement.

The disintegration rate of the sample is obtained as 98% during the initial run which is decreased to 86% at 6th repetitive runs. Fig. 18 reveals the continuous decrease of degradation rate over six continual runs and the change of degradation efficiency is around $\sim 12\%$ following six continuous recycling runs. The probable reason for the above reduction in the degradation efficiency may be due to the loss of catalysts by the drying and washing. The result of this stability measurement signifies that Cu doped $\text{Cd}_{0.9}\text{Zn}_{0.1}\text{S}$ exhibits superior dye removal ability and better stability even after 6 repetitive runs with limited photo-corrosion.

4. Conclusions

Following are the conclusions drawn from the present investigation:

- The controlled synthesis of $\text{Cd}_{0.9}\text{Zn}_{0.1}\text{S}$, $\text{Cd}_{0.89}\text{Zn}_{0.1}\text{Cu}_{0.01}\text{S}$ and $\text{Cd}_{0.87}\text{Zn}_{0.1}\text{Cu}_{0.03}\text{S}$ nanostructures by simple chemical co-precipitation technique was reported.
- The XRD investigation confirmed the basic CdS cubic structure on Zn-doped CdS and also Zn, Cu dual doped CdS with no secondary/impurity related phases.
- No modification in cubic structure was detected during the addition of Zn/Cu into CdS.
- The reduction of crystallite size from 63 \AA to 40 \AA and the changes in lattice parameter confirmed the incorporation of Cu into $\text{Cd}_{0.9}\text{Zn}_{0.1}\text{S}$ and generation of Cu related defects.
- The shift of absorption edge along upper wavelength region and elevated absorption intensity by Cu doping can be accredited to the collective consequence of quantization and the generation of defect associated states.
- The enhanced optical absorbance and the reduced energy gap recommended that $\text{Cd}_{0.87}\text{Zn}_{0.1}\text{Cu}_{0.03}\text{S}$ nanostructure is useful to enhance the efficiency of opto-electronic devices.

- The presence of Cd-S / Zn-Cd-S / Zn/Cu-Cd-S chemical bonding were confirmed by Fourier transform infrared investigation.
- The elevated green emissions by Cu incorporation was explained by decrease of crystallite size and creation of more defects.
- Zn, Cu dual doped CdS nanostructures are recognized as the possible and also efficient photo-catalyst for the removal dyes like methylene blue.
- The enhanced photo-catalytic behaviour of Zn, Cu dual doped CdS is the collective consequences of high density electron-hole pairs creation, enhanced absorbance in the visible wavelength, surface area enhancement, reduced energy gap and the formation of novel defect associated states.
- The stability measurement signified that Cu doped Cd_{0.9}Zn_{0.1}S exhibits superior dye removal ability and better stability even after 6 repetitive runs with limited photo-corrosion.

References

1. K. Deka, P.C. Manos, Kalita, J. Alloys Compd. **757**, 209–220 (2018)
2. S. Abdulwahab, Z. Lahewil, Y. Al-Douri, U. Hashim, N.M. Ahmed, Sol. Energy **86**, 3234 (2012)
3. P.A. Chate, S.S. Patil, J.S. Patil, D.J. Sathe, P.P. Hankare, Synthesis, Phys. B **411**, 118–121 (2013)
4. S.A. Waly, M.M. Shehata, H.H. Mahmoud, Russ. J. Appl. Chem. **90**, 292–297 (2017)
5. A.A. Ibiyemi, A.O. Awodugba, O. Akinrinola, A.A. Faremi, J. Semiconduct. **38**, 093002–093006 (2017)
6. P. Chand, R. Ghosh, Sukriti, Optik **161**, 44–53 (2018)
7. G.F. Zheng, W. Lu, C.M. Lieber, Adv. Mater. **21**, 1890–1893 (2004)
8. Y. Huang, H.F. Duan, C.M. Lieber, Small **1**, 142–147 (2005)
9. T.T. Xuan, J.Q. Liu, R.J. Xie, H.L. Li, Z. Sun, Chem. Mater. **27**, 1187–1193 (2015)
10. Y. Zhang, S. Deng, J. Lei, Q. Xu, H. Ju, Talanta **85**, 2154–2158 (2011)
11. W. Wondmagegn, I. Mejia, A. Salas-Villasenor, H. Stiegler, M. Quevedo-Lopez, R. Pieper, B. Gnade, Microelectron. Eng. **157**, 64–70 (2016)
12. X. Zong, H. Yan, G. Wu, G. Ma, F. Wen, L. Wang, C. Li, J. Am. Chem. Soc. **130**, 7176–7177 (2008)
13. X. Yang, Z. Wang, X. Lv, Y. Wang, H. Jia, J. Photochem. Photobiol. A Chem. **329**, 175–181 (2016)
14. M. Ueta, H.B. Kanzaki, K. Kobayashi, Y. Toyozawa, E. Hanamura, Excitonic processes in solids, in: Springer Series in Solid State Sciences, Vol. 60, Springer, Berlin, 1986
15. F. Yang, N.N. Yan, H. Sheng, Q. Sun, L.Z. Zhang, Y. Yu, J. Phys. Chem. C **116**, 9078–9084 (2012)
16. Q. Li, B.D. Guo, J.G. Yu, J.R. Ran, B.H. Zhang, J. Am. Chem. Soc. **133**, 10878–10884 (2011)
17. A.H. Mueller, M.A. Petruska, M. Achermann, D. Werder, E. Akhadov, D. Koleske, M. Hoffbauer, V.I. Klimov, Nano Lett. **5**(6), 1039–1044 (2005)
18. Z.K. Heiba, M.B. Mohamed, N.G. Imam, J. Mol. Struct. **1136**, 321–329 (2017)
19. N.G. Imam, M.B. Mohamed, J. Mol. Struct. **1105**, 80–86 (2016)

20. Z.K. Heiba, M.B. Mohamed, N.G. Imam, *Ceram. Int.* **41**(10), 12930–12938 (2015)
21. G. Laukaitis, S. Lindroos, S. Tamulevicius, M. Leskela, M. Rackaitis, *Appl. Surf. Sci.* **161**, 396–405 (2000)
22. L. Ma, X. Ai, X. Wu, *J. Alloys Compd.* **691**, 399–406 (2017)
23. P. Elavarthi, A.A. Kumar, G. Murali, D.A. Reddy, K.R. Gunasekhar, *J. Alloys Compd.* **656**, 510–517 (2016)
24. R. Banerjee, R. Jayakrishnan, P. Ayyub, *J. Phys. Condens. Matter* **12**(50), 10647–10654 (2000)
25. P.S. Chowdhury, A. Patra, *Phys. Chem. Chem. Phys.* **8**, 1329–1334 (2006)
26. T. Trindade, P. O'Brien, N.L. Pickett, *Chem. Mater.* **13**, 3843–3858 (2001)
27. H. Khallaf, G. Chai, O. Lupan, L. Chow, S. Park, A. Schulte, *Appl. Surf. Sci.* **255** (2009) 4129–4134
28. P. Roy, S.K. Srivastava, *J. Phys. D Appl. Phys.* **39**, 4771 (2006)
29. J.-H. Lee, J.-S. Yi, K.-J. Yang, J.-H. Park, R.-D. Oh, *Thin Solid Films* **431**, 344–348 (2003)
30. P. Sebastian, *Appl. Phys. Lett.* **62**, 2956–2958 (1993)
31. P. George, A. Sanchez, P. Nair, M. Nair, *Appl. Phys. Lett.* **66**, 3624–3626 (1995)
32. J. Jayaramaiah, R. Shamanth, V. Jayanth, K. Shamala, *Curr. Appl. Phys.* **16**, 799–804 (2016)
33. A. Mukherjee, M. Fu, P. Mitra, *J. Phys. Chem. Solids* **82**, 50–55 (2015)
34. M.A. Baghchesara, R. Yousefi, M. Cheraghizade, F. Jamali-Sheini, A. Saaedi, *Ceram. Int.* **42**, 1891–1896 (2016)
35. H. Sekhar, D.N. Rao, *J. Mater. Sci.* **47**, 1964–1971 (2012)
36. S.J.C. Irvine, V. Barrioz, D. Lamb, E.W. Jones, R.L. Rowlands-Jones, *J. Cryst. Growth* **310**, 5198–5203 (2008)
37. M. Anpo, M. Takeuchi, *J. Catal.* **216**, 505–516 (2003)
38. I. Devadoss, S. Muthukumaran, M. Ashokkumar, *J. Mater. Sci.* **25**, 3308–3317 (2014)
39. Y. Kashiwaba, K. Isojima, K. Ohta, *Sol. Energy Mater. Sol. Cells* **75**, 253–259 (2003)
40. D. Petre, I. Pintilie, E. Pentia, I. Pintilie, T. Botila, *Mater. Sci. Eng., B* **58**, 238–243 (1999)
41. Y. Kashiwaba, I. Kanno, T. Ikeda, *Jpn. J. Appl. Phys.* **31**, 1170–1175 (1992)
42. S. Linsi, B. Kavitha, M. Dhanam, B. Maheswari, *J. World Appl. Sci.* **10** (2010), 207–213
43. G. Liu, Z. Zhou, L. Guo, *Chem. Phys. Lett.* **509**, 43–47 (2011)
44. R. Singh, S. Basu, B. Pal, *Mater. Res. Bull.* **94**, 279–286 (2017)
45. A. Khare, S. Bhushan, *Radiat. Effects Defects Solids* **161**, 631–644 (2006)
46. H. Ye, A.J. Freeman, B. Delley, *Phys. Rev. B* **73**, 033203 (2006)
47. H. Liu, J. Yang, Z. Hua, Y. Zhang, L. Yang, L. Xiao, Z. Xie, *Appl. Surf. Sci.* **256**, 4162–4165 (2010)
48. M. Muthusamy, S. Muthukumaran, *Optik* **126**, 5200–5206 (2015)
49. R. Mariappan, V. Ponnuswamy, M. Ragavendar, D. Krishnamoorthi, C. Sankar, *Optik* **123**, 1098–1102 (2012)

50. Z. Sedaghat, N. Tagavinia, M. Marandi, *Nanotechnology* **17**, 3812–3817 (2006)
51. E. Dutkova, P. Balaz, P. Pourghahramani, A.V. Nguyen, V. Sepelak, A. Feldhoff, J. Kovac, A. Satka, *Solid State Ion.* **179**, 1242–1245 (2008)
52. S. Muruganandam, G. Anbalagan, G. Murugadoss, *Optik* **130**, 82–90 (2017)
53. B.D. Cullity, *Elements of X-ray Diffraction* (Addison Wesley, USA, 1978)
54. S. Anandan, S. Muthukumar, M. Ashokkumar, *Superlattices Microstruct.* **74**, 247–260 (2014)
55. X.L. Yang, Z.T. Chen, C.D. Wang, Y. Zhang, X.D. Pei, Z.J. Yang, G.Y. Zhang, Z.B. K. Ding, S.D. Wang, Yao, *J. Appl. Phys.* **105**, 053910 (2009)
56. M. Shaban, M. Mustafa, A.M. El, Sayed, *Mater. Sci. Semicond. Process.* **56**, 329–343 (2016)
57. J. Pelleg, E. Elish, *J. Vac. Sci. Technol. A* **20**, 754–761 (2002)
58. M. Ashokkumar, S. Muthukumar, *J. Lumin.* **145**, 167–174 (2014)
59. J. Woltersdorf, A. Nepijko, E. Pippel, *Surf. Sci.* **106**, 64–69 (1981)
60. I. Devadoss, S. Muthukumar, *Physica E* **72**, 111–119 (2015)
61. M. Muthusamy, S. Muthukumar, M. Ashokkumar, *Ceramics Inter.* **40**, 10657–10666 (2014)
62. I. Devadoss, P. Sakthivel, S. Muthukumar, N. Sudhakar, *Ceram. Int.* **45**, 3833–3838 (2019)
63. X. Qiu, M. Miyauchi, H. Yu, H. Irie, K. Hashimoto, *J. Am. Chem. Soc.* **132** (2010), 15259–15267
64. J. Sun, G. Chen, Y. Li, C. Zhao, H. Zhang, *J. Alloys Compd.* **509**, 1133–1137 (2011)
65. H. Khallaf, I.O. Oladeji, L. Chow, *Thin Solid Films* **516**, 5967–5973 (2008)
66. A.A. Ziabari, F.E. Ghodsi, *J. Mater. Sci.: Mater. Electron.* **23**, 1628–1633 (2012)
67. F. Liu, Y. Lai, J. Liu, B. Wang, S. Kuang, Z. Zhang, J. Li, Y. Liu, *J. Alloys Compd.* **493**, 305–308 (2010)
68. J.J. Tauc, R. Grigorovici, A. Vancu, *Phys. Status Solidi* **15**, 627–637 (1966)
69. K.S. Kumar, A. Divya, P.S. Reddy, *Appl. Surf. Sci.* **257**, 9515–9518 (2011)
70. M. Elango, K. Gopalakrishnan, S. Vairam, M. Thamilselvan, *J. Alloys Compd.* **538**, 48–55 (2012)
71. P.J. Sebastian, M. Ocampo, *J. Appl. Phys.* **77**, 4548–4551 (1995)
72. P. Reyes, F. Velumani, *Mater. Sci. Engg. B* **177**, 1452 (2012)
73. H. Kato, J. Sato, T. Abe, Y. Kashiwaba, *Phys. Status Solidi (C)* **1** (2004) 653
74. S. Aksu, E. Bacaksiz, M. Parlak, S. Yilmaz, I. Polat, M. Altunbas, M. Turksoy, R. Topkaya, K. Ozdogan, *Mater. Chem. Phys.* **130**, 340–345 (2011)
75. S.Y. Li, P. Lin, C.Y. Lee, T.Y. Tseng, *J. Appl. Phys.* **95**, 3711–3716 (2004)
76. P.K. Sharma, M. Kumar, A.C. Pandey, *J. Nanopart. Res.* **13**, 1629–1637 (2011)
77. A. Goktas, I.H. Mutlu, *J. Elec. Mater.* **45**, 5709–5720 (2016)
78. F.L. Xian, L.H. Xu, X.X. Wang, X.Y. Li, *Cryst. Res. Technol.* **47**, 423–428 (2012)
79. L.R. Valerio, N.C. Mamani, A.O. de Zevallos, A. Mesquita, M.I.B. Bernardi, A.C. Doriguetto, H.B. de Carvalho, *RSC Adv.* **7**, 20611–20619 (2017)
80. B. Malinowska, M. Rakib, G. Durand, *Sol. Cells* **86**, 399–419 (2005)

81. M.F. Kotkata, A.E. Masoud, M.B. Mohamed, E.A. Mahmoud, *Physica E* **41**, 1457–1465 (2009)
82. K.M.K. Selim, I.-K. Kang, H. Guo, *Macromol. Res.* **17**, 403–410 (2009)
83. X. Sun, X. Ma, L. Bai, J. Liu, Z. Chang, D.G. Evans, X. Duan, J. Wang, J.F. Chiang, *Nano Res.* **4**, 226–232 (2011)
84. R. Heitz, A. Hoffmann, I. Broser, *Phys. Rev. B* **48**, 8672–8682 (1993)
85. N. Chestnoy, T.D. Harris, R. Hull, L.E. Brus, *J. Phys. Chem.* **90**, 3393–3399 (1986)
86. Y. Wang, N.J. Herron, *J. Phys. Chem.* **92**, 4988–4994 (1988)
87. S. Arora, S.S. Manoharan, *Solid State Comm.* **144**, 319–323 (2007)
88. H. Huang, X. Han, X.W. Li, S. Wang, P.K. Chu, Y. Zhang, *ACS Appl. Mater. Interfaces* **7**, 482–492 (2015)
89. R. Panda, V. Rathore, M. Rathore, V. Shelke, N. Badera, L.S. Sharath Chandra, D. Jain, M. Gangrade, T. Shripati, V. Ganesan, *Appl. Surf. Sci.* **258**, 5086–5093 (2012)
90. R. Atchudan, T.N.J.I. Edison, S. Perumal, D. Karthikeyan, Y.R. Lee, *J. Photochem. Photobiol. B* **162**, 500–510 (2016)
91. C.B. Ong, L.Y. Ng, A.W. Mohammad, *Renew. Sustain. Energy Rev.* **81**, 536–551 (2018)
92. R.M. Navarro, M.C. Alvarez-Galvan, J.A.V. de la Mano, S.M. Al-Zahrani, J.L.G. Fierroa, *Energy Environ. Sci.* **3**, 1865–1882 (2010)
93. B. Ahmed, A.K. Ojha, S. Kumar, *Spectrochim. Acta A Mol. Biomol. Spectrosc.* **179**, 144–154 (2017)
94. J. Wu, Z. Li, F. Li, *Superlattice Microstruct.* **54**, 146–154 (2013)
95. K. Karthik, S. Dhanuskodi, S. Prabukumar, C. Gobinath, S. Sivaramakrishnan, *J. Mater. Sci.: Mater. Electron.* **29**, 5459–5471 (2018)
96. K. Milenova, I. Stambolova, V. Blaskov, A. Eliyas, S. Vassilev, M. Shipochka, *J. Chem. Technol. Metal.* **48**, 259–264 (2013)
97. M. Rezapour, N. Talebian, *Mater. Chem. Phys.* **129**, 249–255 (2011)
98. C. Rajendra, C.S. Pawar, Lee, *Appl. Catal. B- Environ.* **144**, 57–65 (2014)

Tables

Table 1

The peak position (2 θ value), FWHM value, d-value, cell parameter 'a', crystallite size (D) and micro-strain (e) of Cd_{0.9-x}Zn_{0.1}Cu_xS (x = 0, 0.01 and 0.03) nanostructures

Samples	Peak position 2θ ($^{\circ}$)	FWHM (β) (degrees)	d value (\AA)	Cell parameter $a = b = c$ (\AA)	Average Crystallite size (D) (\AA)	Micro-strain (e) (10^{-3})
$\text{Cd}_{0.9}\text{Zn}_{0.1}\text{S}$	27.15	1.29	3.281	5.683	63	5.471
$\text{Cd}_{0.89}\text{Zn}_{0.1}\text{Cu}_{0.01}\text{S}$	26.56	1.76	3.353	5.810	46	7.474
$\text{Cd}_{0.87}\text{Zn}_{0.1}\text{Cu}_{0.03}\text{S}$	26.67	2.04	3.340	5.780	40	8.661

Table 2

The quantitative analysis of atomic percentage of the compositional elements presents in $\text{Cd}_{0.9-x}\text{Zn}_{0.1}\text{Cu}_x\text{S}$ ($x = 0, 0.01$ and 0.03) nanoparticles using EDX analysis

Samples	Atomic percentage of the elements (%)				Cu/(Cd+Zn+Cu) ratio (%)
	Cd	S	Cu	Zn	
$\text{Cd}_{0.9}\text{Zn}_{0.1}\text{S}$	53.02	41.36	-	5.62	-
$\text{Cd}_{0.89}\text{Zn}_{0.1}\text{Cu}_{0.01}\text{S}$	52.03	41.81	0.57	5.59	0.98
$\text{Cd}_{0.87}\text{Zn}_{0.1}\text{Cu}_{0.03}\text{S}$	51.58	41.01	1.78	5.63	3.02

Table 3

IR peaks and their assignments of $\text{Cd}_{0.9-x}\text{Zn}_{0.1}\text{Cu}_x\text{S}$ ($x = 0, 0.01$ and 0.03) nanostructures at room temperature

Assignments	Wave number (cm^{-1})		
	$\text{Cd}_{0.9}\text{Zn}_{0.1}\text{S}$	$\text{Cd}_{0.89}\text{Zn}_{0.1}\text{Cu}_{0.01}\text{S}$	$\text{Cd}_{0.87}\text{Zn}_{0.1}\text{Cu}_{0.03}\text{S}$
O-H stretching vibration of H_2O	3480	3396	3493
H-O-H bending vibration of H_2O	1610	1592	1631
Cu induced micro-structural changes	842	793	861
Stretching mode of Cd-Zn-S (doublet)	432, 671	428, 683	431, 685

Figures

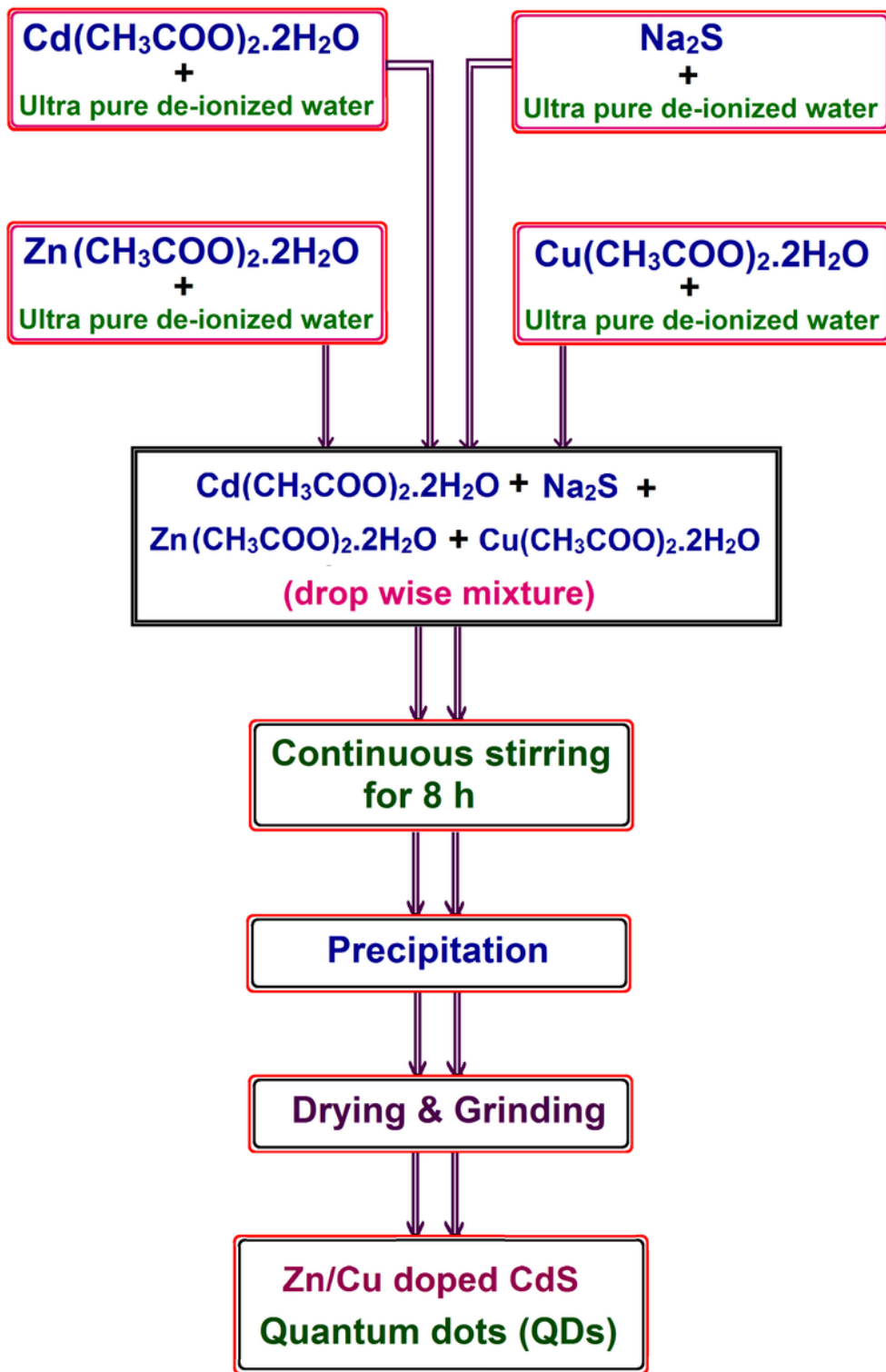


Figure 1

Flowchart and the preparation steps for the preparation of Zn and Cu dual doped CdS nanostructures using chemical precipitation method.

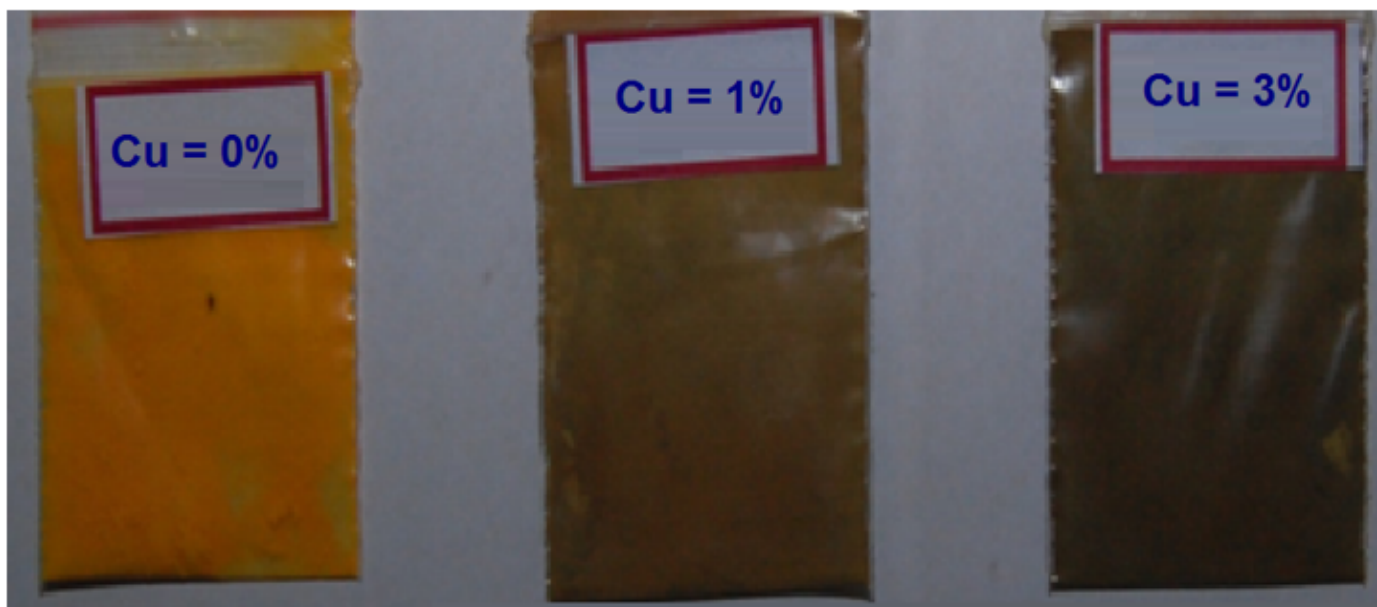


Figure 2

The color of change of Cd_{0.9}Zn_{0.1}S nanostructure from yellow to light brown and brown for Cu = 1 and 3% doped Cd_{0.9}Zn_{0.1}S, respectively.

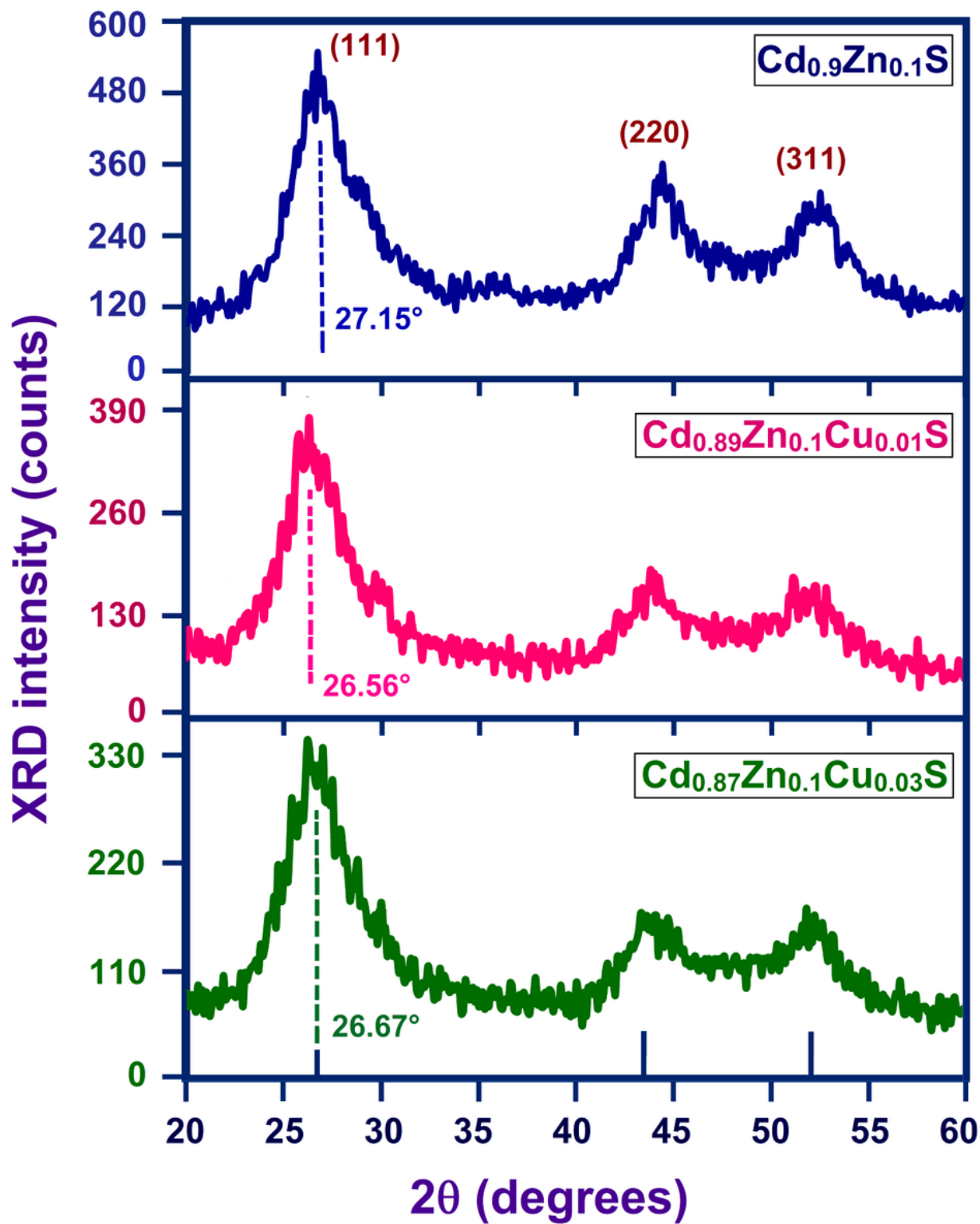


Figure 3

XRD pattern of $\text{Cd}_{0.9}\text{Zn}_{0.1}\text{S}$, $\text{Cd}_{0.89}\text{Zn}_{0.1}\text{Cu}_{0.01}\text{S}$ and $\text{Cd}_{0.87}\text{Zn}_{0.1}\text{Cu}_{0.03}\text{S}$ nanostructures between 20° and 60° .

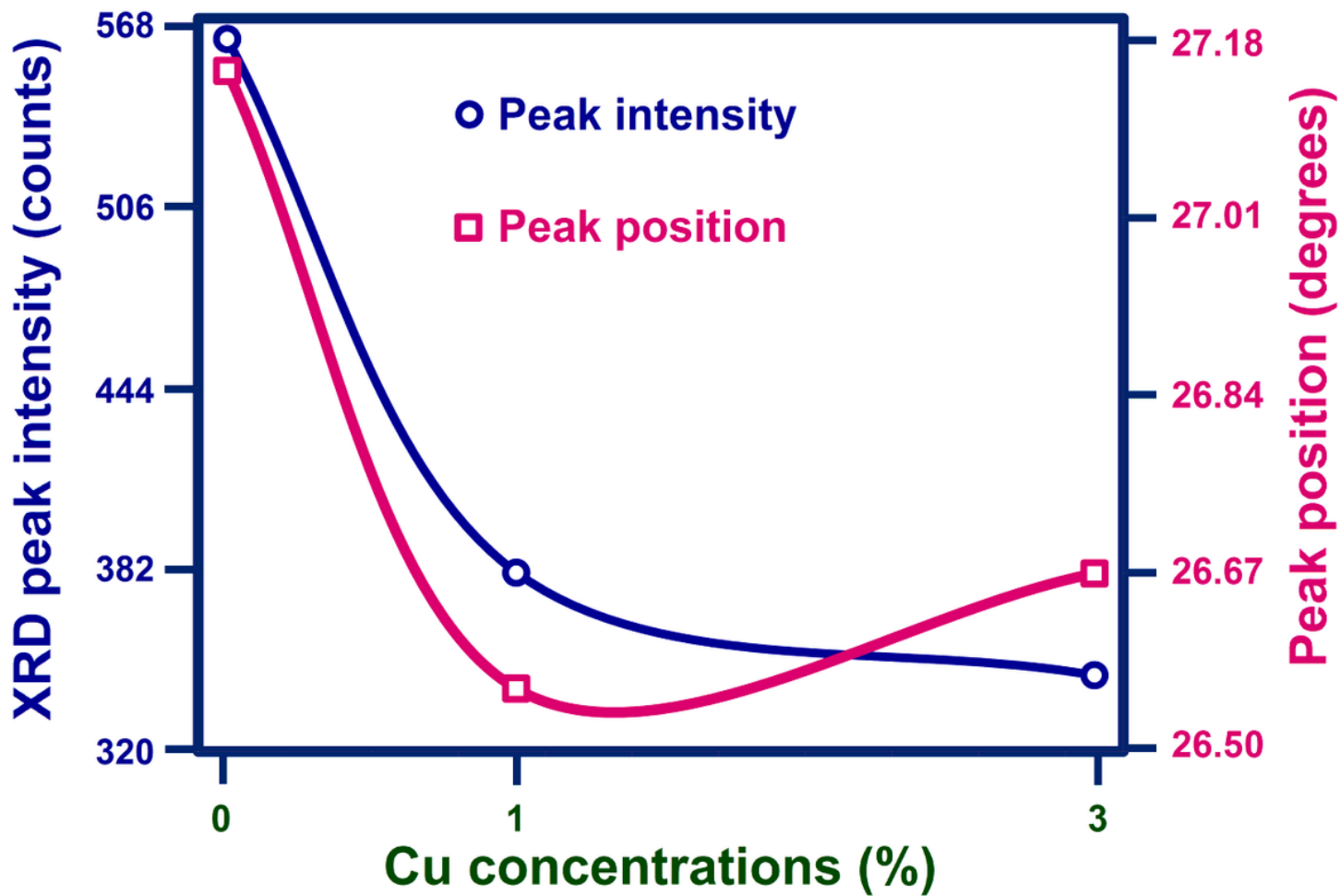


Figure 4

Variation of XRD peak intensity and peak position along (111) orientation of Cd_{0.9}Zn_{0.1}S nanostructure for different Cu concentrations from 0 to 3%.

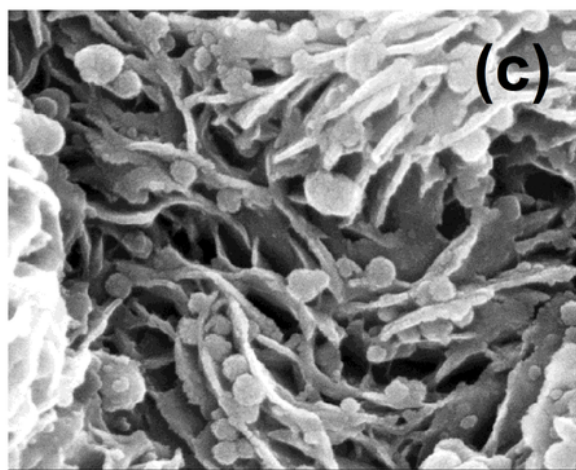
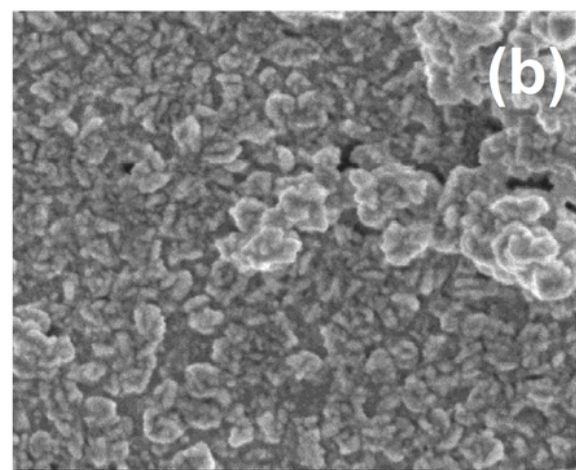
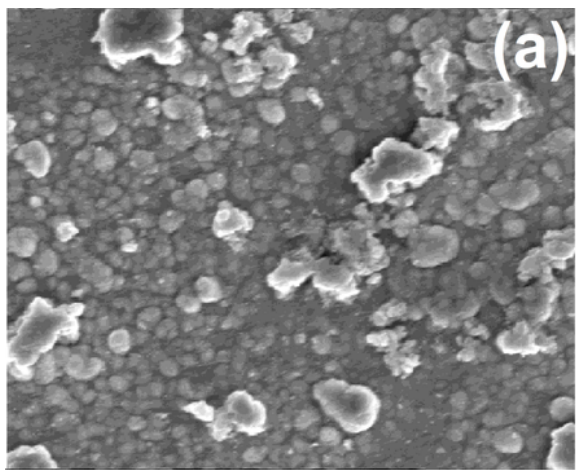


Figure 5

SEM micrographs of (a) $\text{Cd}_{0.9}\text{Zn}_{0.1}\text{S}$, (b) $\text{Cd}_{0.89}\text{Zn}_{0.1}\text{Cu}_{0.01}\text{S}$ and (c) $\text{Cd}_{0.87}\text{Zn}_{0.1}\text{Cu}_{0.03}\text{S}$ nanostructures.

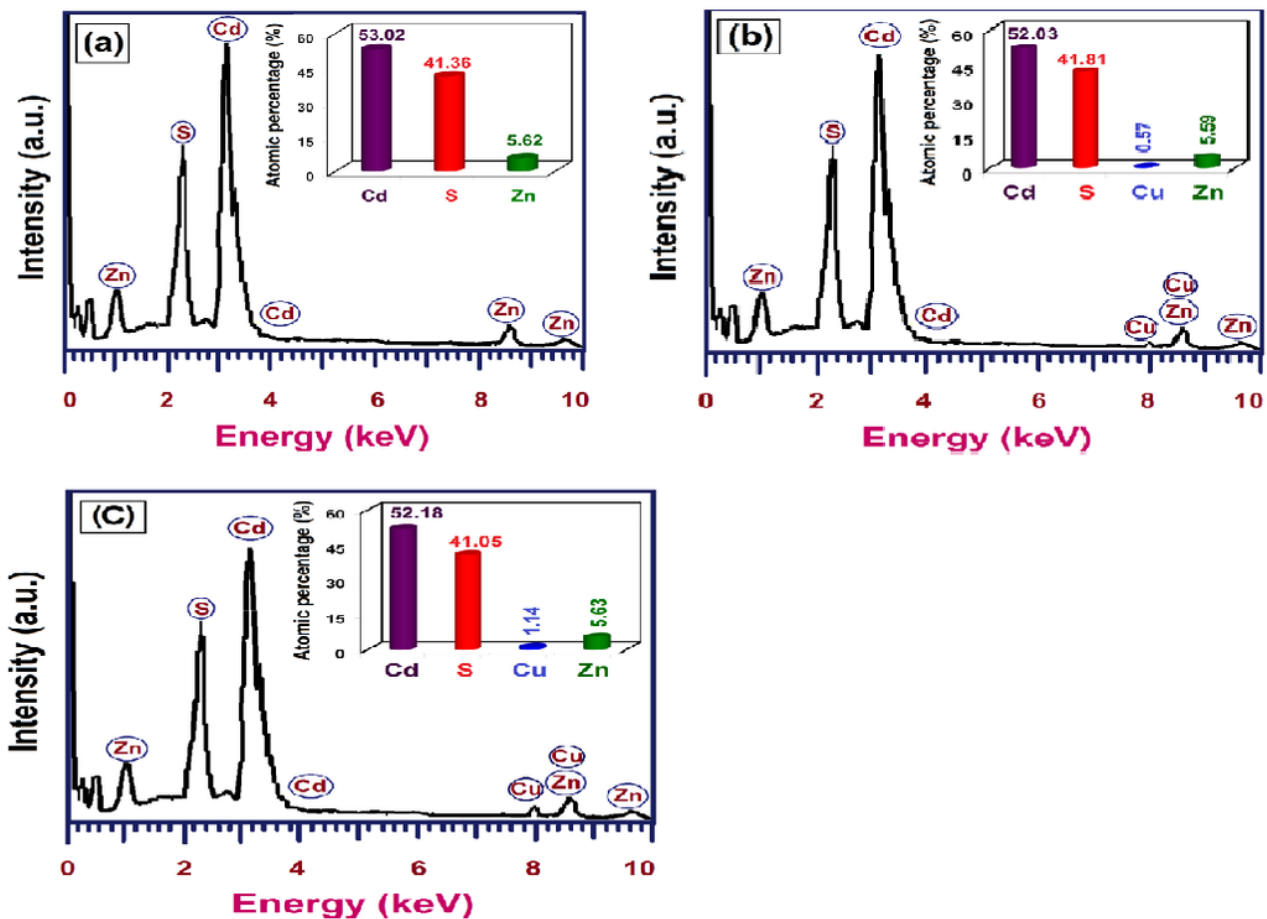


Figure 6

Energy dispersive X-ray (EDX) spectra of (a) Cd_{0.9}Zn_{0.1}S, (b) Cd_{0.89}Zn_{0.1}Cu_{0.01}S and (c) Cd_{0.87}Zn_{0.1}Cu_{0.03}S nanostructures. The inset shows the atomic percentage of constitutional elements like Cd, S, Zn and Cu.

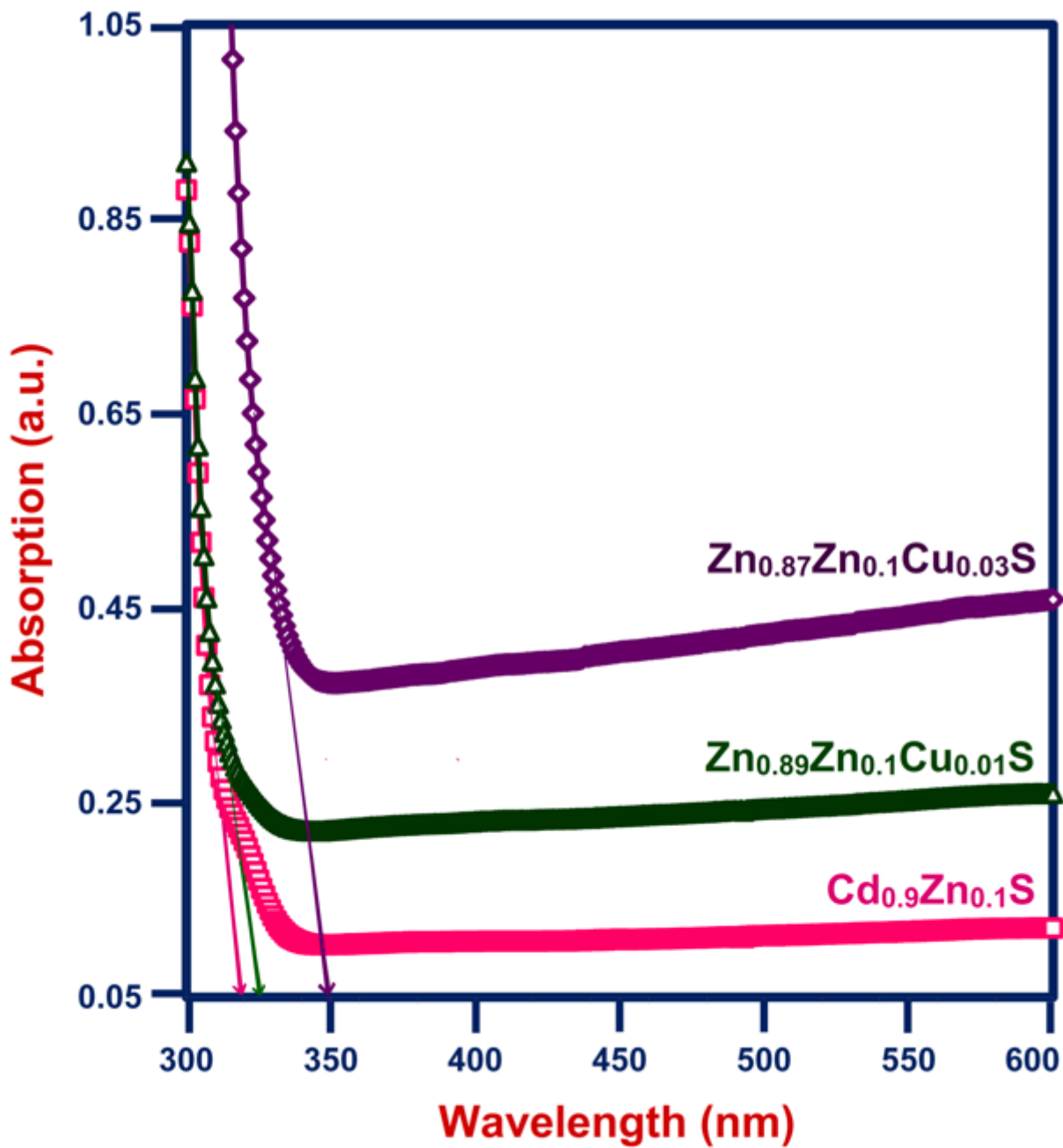


Figure 7

UV-Visible absorption spectra of $\text{Cd}_{0.9}\text{Zn}_{0.1}\text{S}$, $\text{Cd}_{0.89}\text{Zn}_{0.1}\text{Cu}_{0.01}\text{S}$ and $\text{Cd}_{0.87}\text{Zn}_{0.1}\text{Cu}_{0.03}\text{S}$ nanostructures from 300 nm to 600 nm.

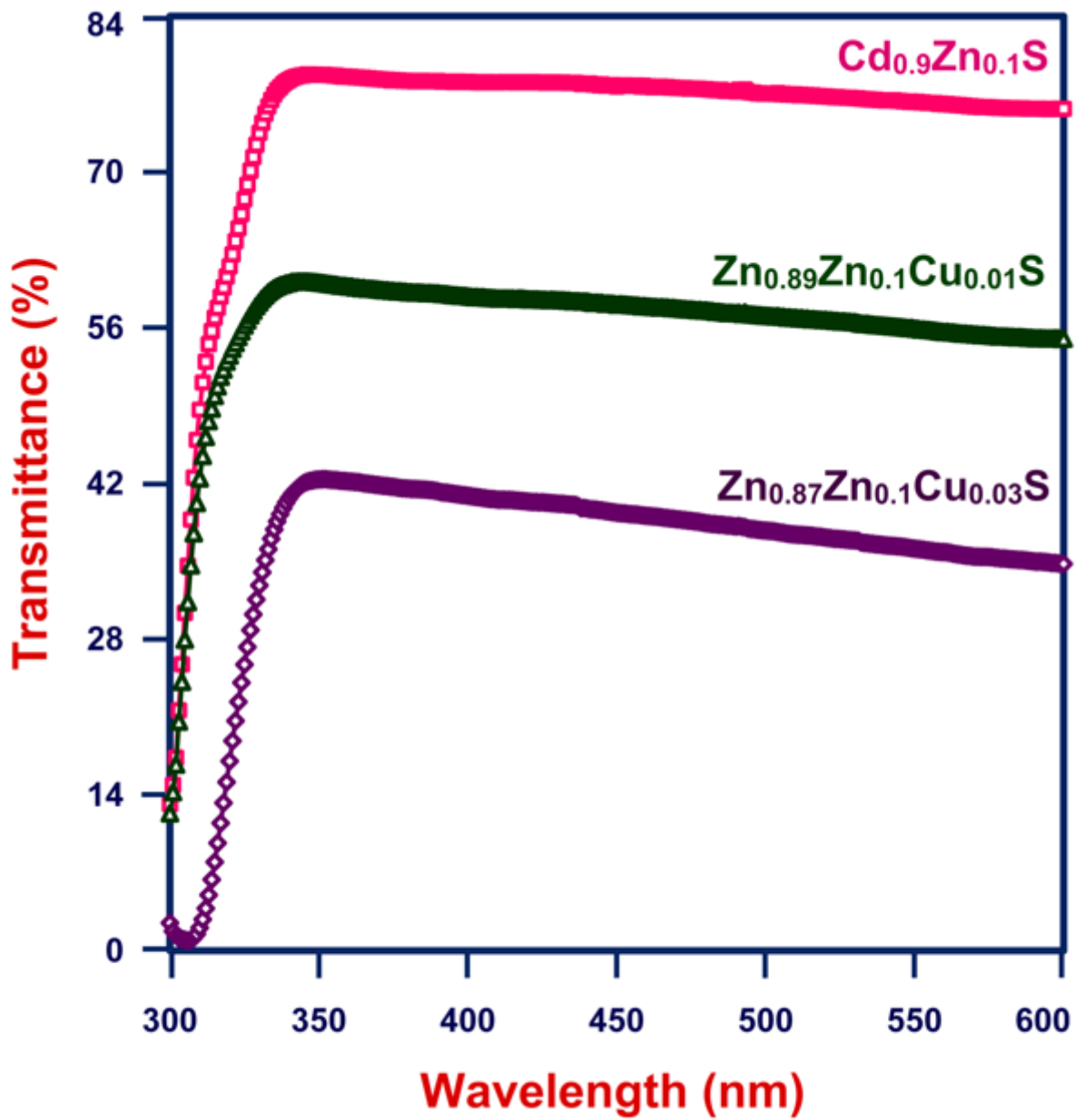


Figure 8

UV-Visible transmittance spectra of Cd_{0.9}Zn_{0.1}S, Cd_{0.89}Zn_{0.1}Cu_{0.01}S and Cd_{0.87}Zn_{0.1}Cu_{0.03}S nanostructures from 300 nm to 600 nm.

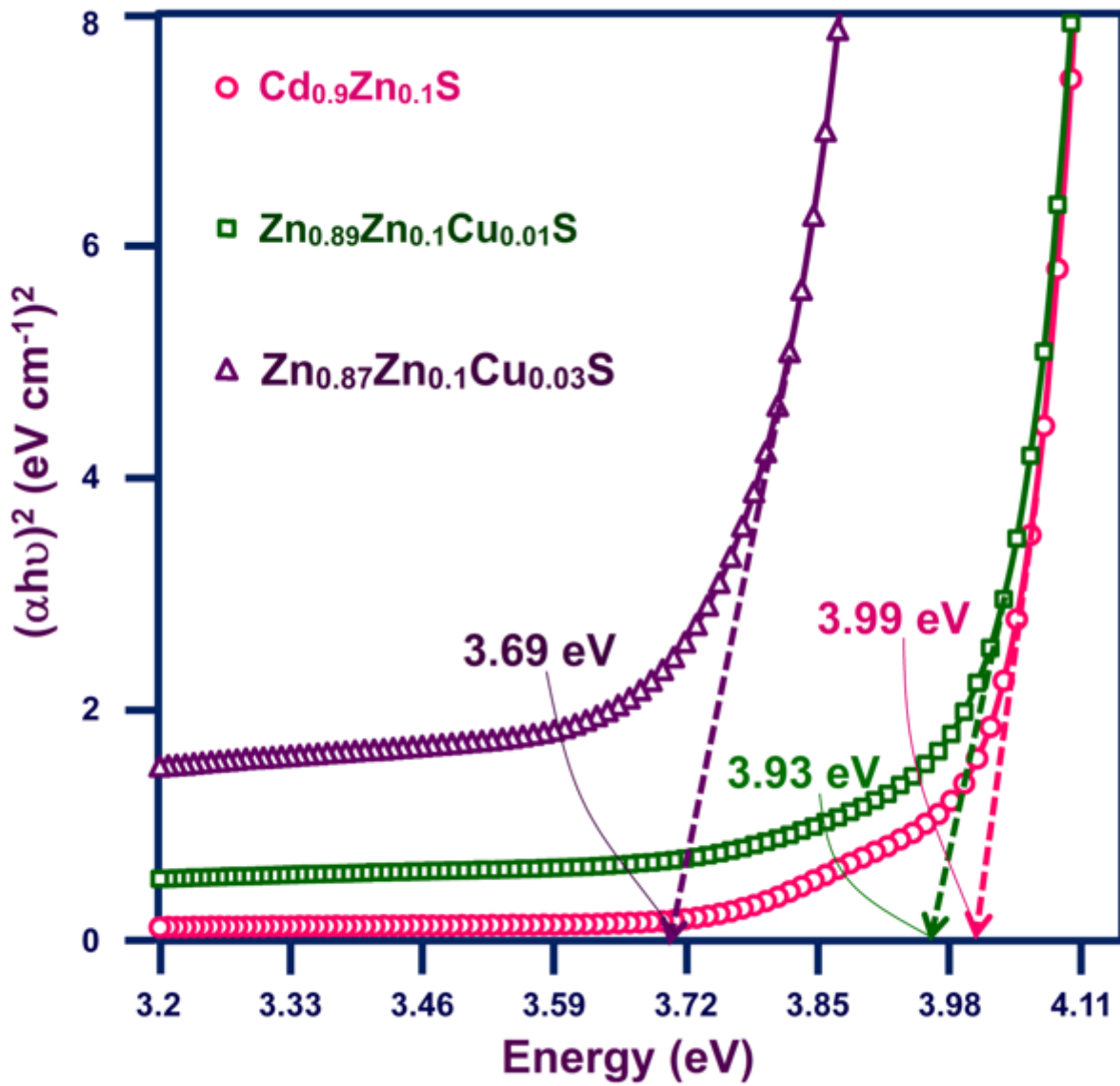


Figure 9

The $(\alpha h\nu)^2$ versus $h\nu$ curves of $\text{Cd}_{0.9}\text{Zn}_{0.1}\text{S}$, $\text{Cd}_{0.89}\text{Zn}_{0.1}\text{Cu}_{0.01}\text{S}$ and $\text{Cd}_{0.87}\text{Zn}_{0.1}\text{Cu}_{0.03}\text{S}$ nanostructures for energy gap estimation.

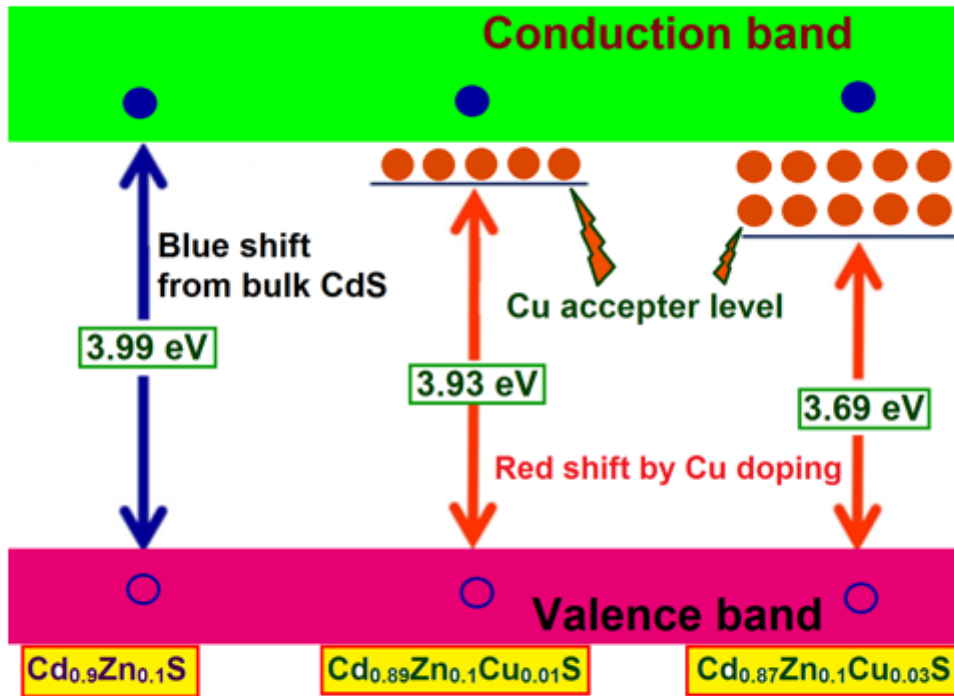


Figure 10

Schematic energy level diagram to explain the red shift of energy gap by Cu addition in $\text{Cd}_{0.9}\text{Zn}_{0.1}\text{S}$ nanostructures.

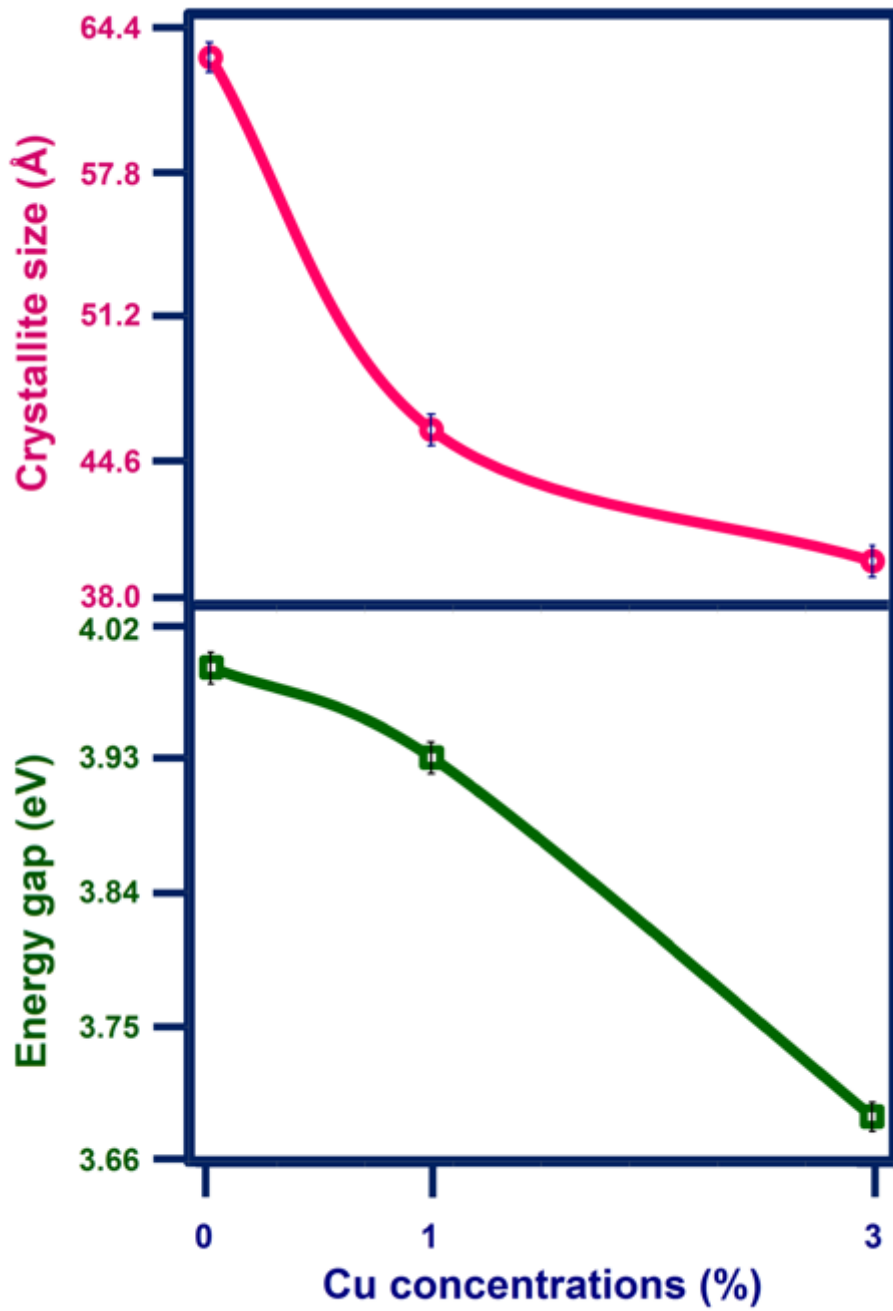


Figure 11

The alteration in crystallite size and energy gap of Cd_{0.9}Zn_{0.1}S nanostructures with different Cu concentrations from 0 to 3%.

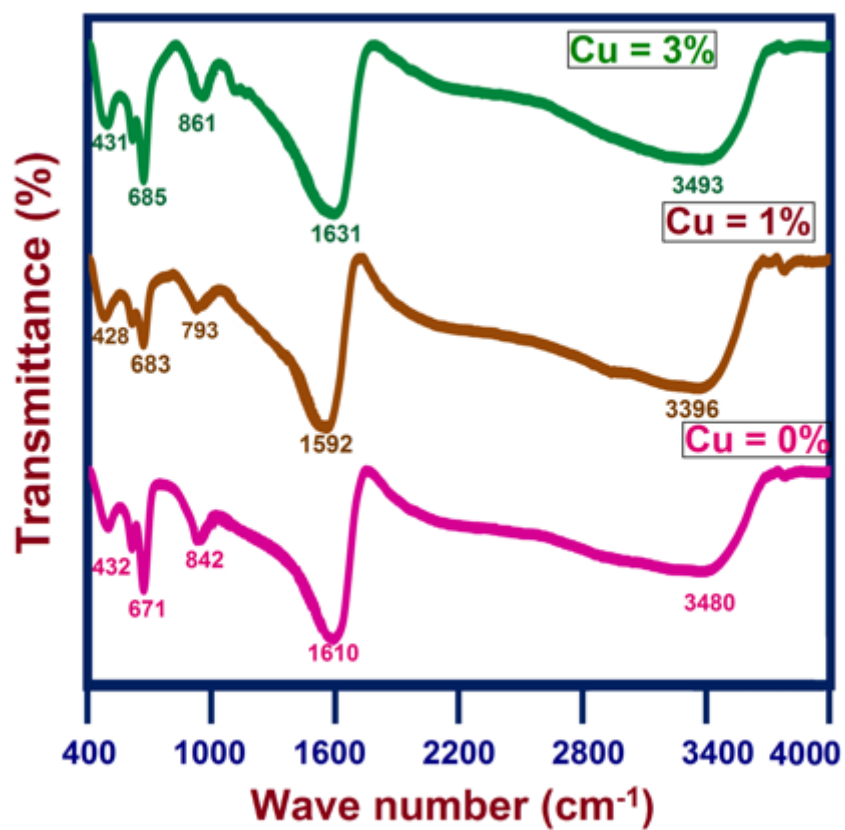


Figure 12

FTIR spectra of $\text{Cd}_{0.9}\text{Zn}_{0.1}\text{S}$, $\text{Cd}_{0.89}\text{Zn}_{0.1}\text{Cu}_{0.01}\text{S}$ and $\text{Cd}_{0.87}\text{Zn}_{0.1}\text{Cu}_{0.03}\text{S}$ nanostructures in the wave number from 400 cm^{-1} to 4000 cm^{-1} at room temperature.

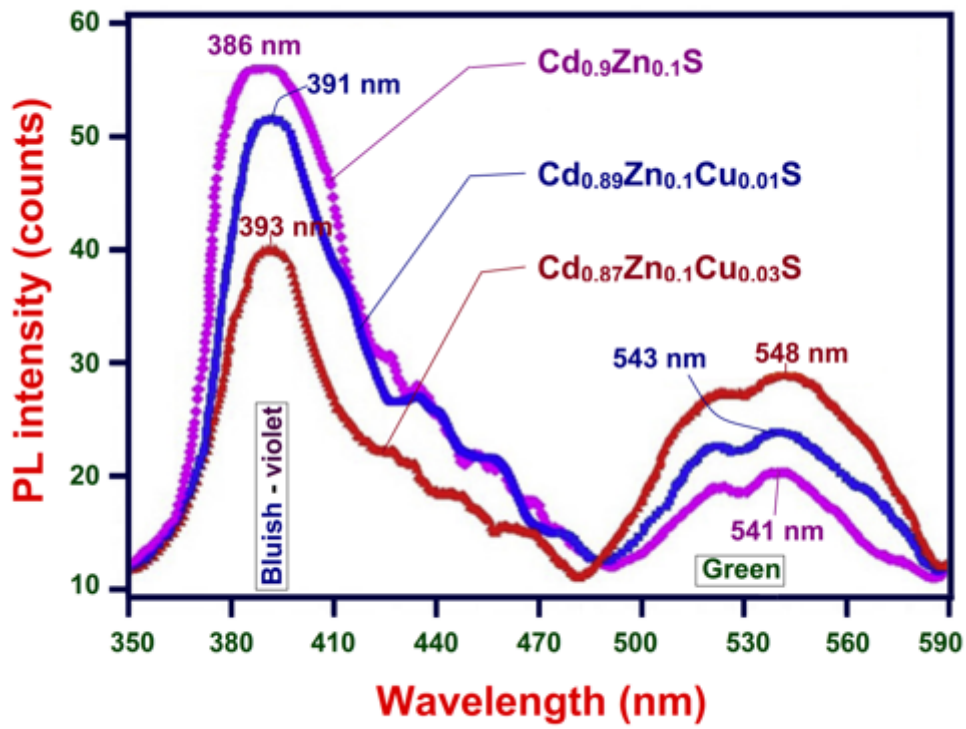


Figure 13

The room temperature PL spectra of $\text{Cd}_{0.9}\text{Zn}_{0.1}\text{S}$, $\text{Cd}_{0.89}\text{Zn}_{0.1}\text{Cu}_{0.01}\text{S}$ and $\text{Cd}_{0.87}\text{Zn}_{0.1}\text{Cu}_{0.03}\text{S}$ nanostructures between 350 nm and 590 nm.

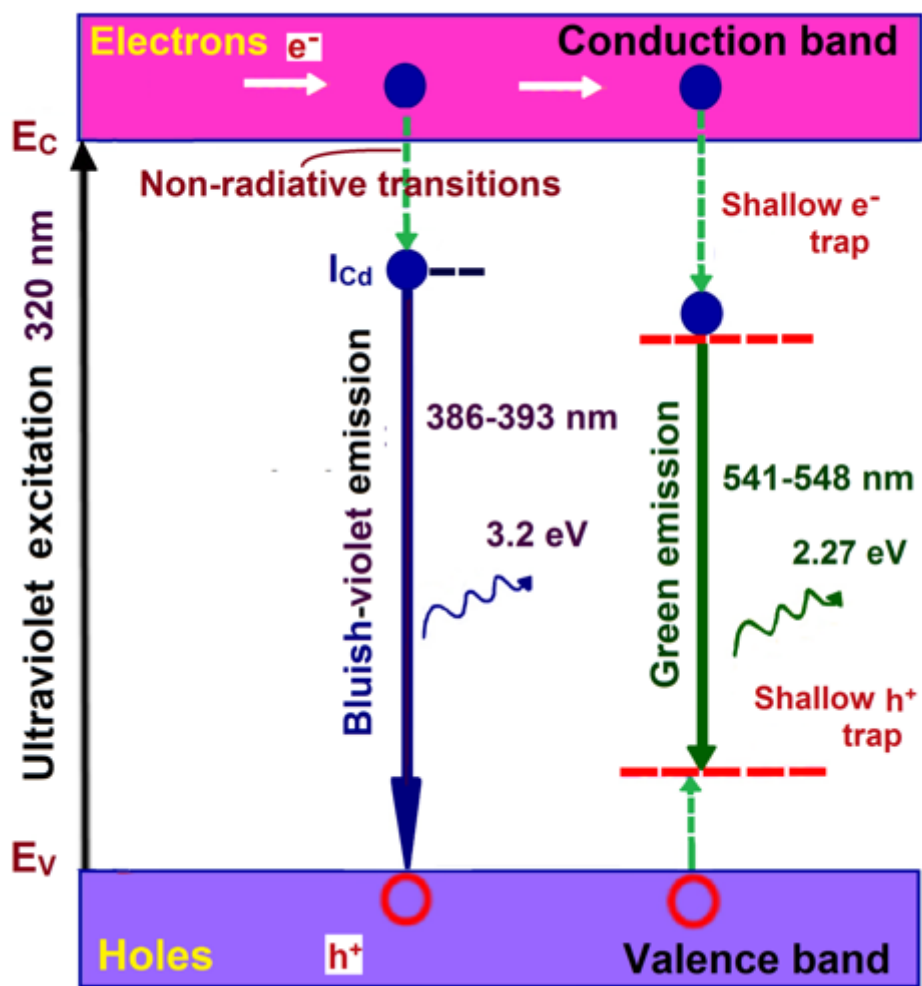


Figure 14

Energy level diagram to explain different emissions like bluish-violet and green emissions in Cd_{0.9-x}Zn_{0.1}Cu_xS (x = 0, 0.01 and 0.03) nanostructures.

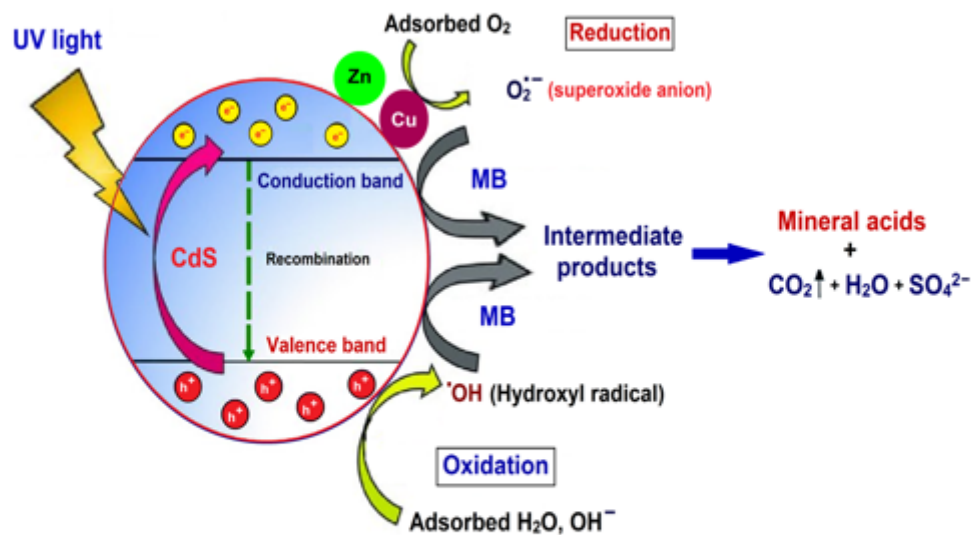


Figure 15

The graphical representation of the photo-catalytic mechanism of Zn/Cu dual doped CdS nanostructures as a catalysts.

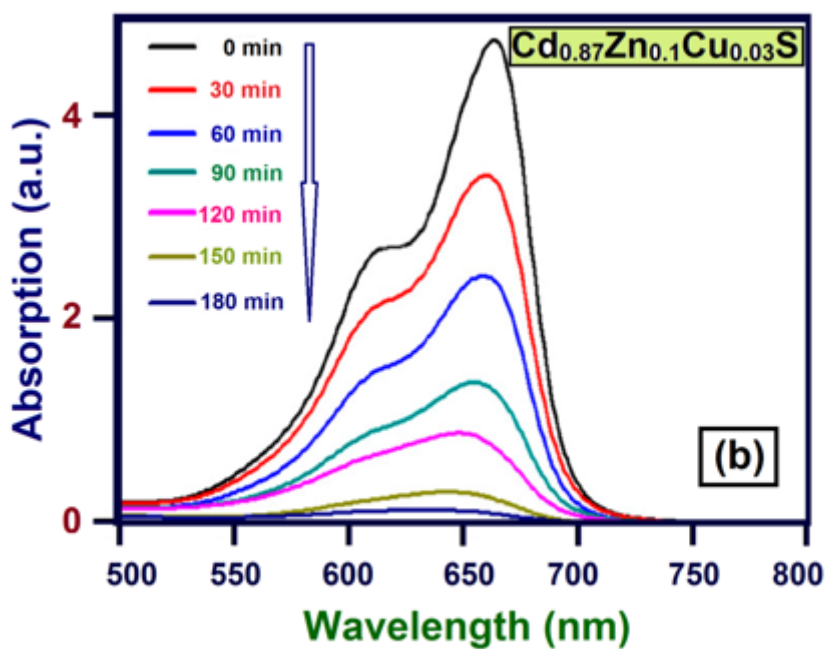
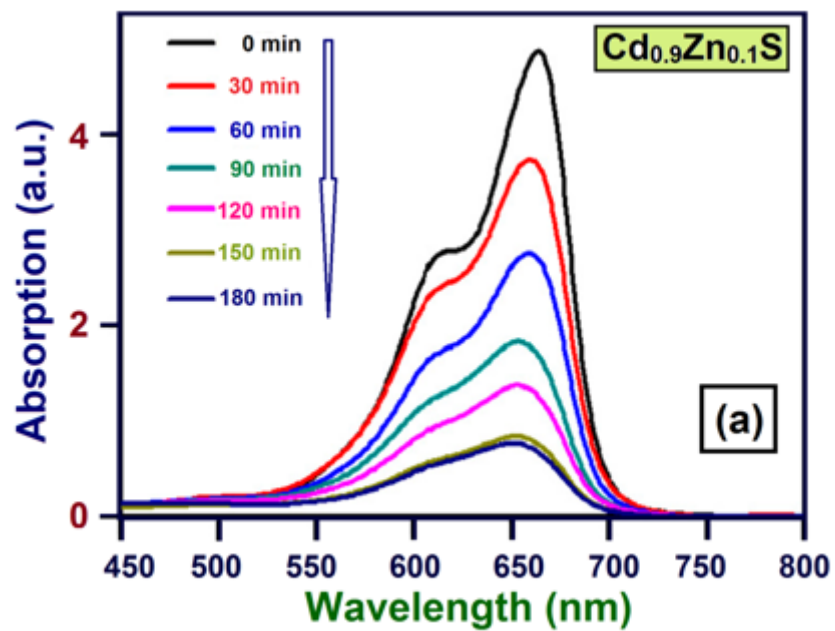


Figure 16

The variation of absorption intensity of MB solution using $\text{Cd}_{0.9}\text{Zn}_{0.1}\text{S}$ and $\text{Cd}_{0.87}\text{Zn}_{0.1}\text{Cu}_{0.03}\text{S}$ nanostructures as a catalysts as a function of wavelength from 450 nm to 800 nm.

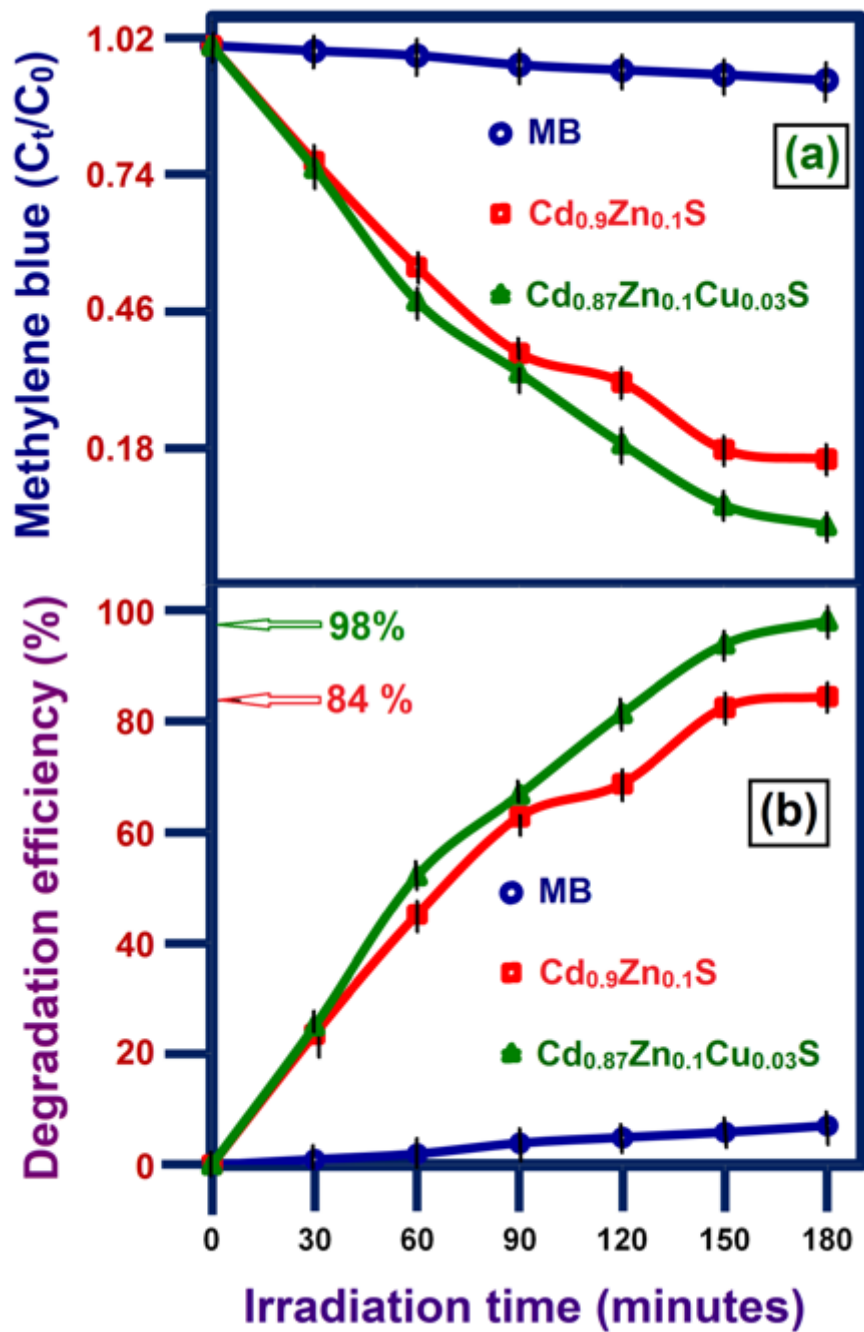


Figure 17

(a) Methylene blue (MB) concentration ratio (C_t/C_0) versus irradiation time profile from 0-180 minutes and (b) degradation efficiency of MB of $Cd_{0.9}Zn_{0.1}S$ and $Cd_{0.87}Zn_{0.1}Cu_{0.03}S$ nanostructures for different light exposure times from 0-180 minutes.

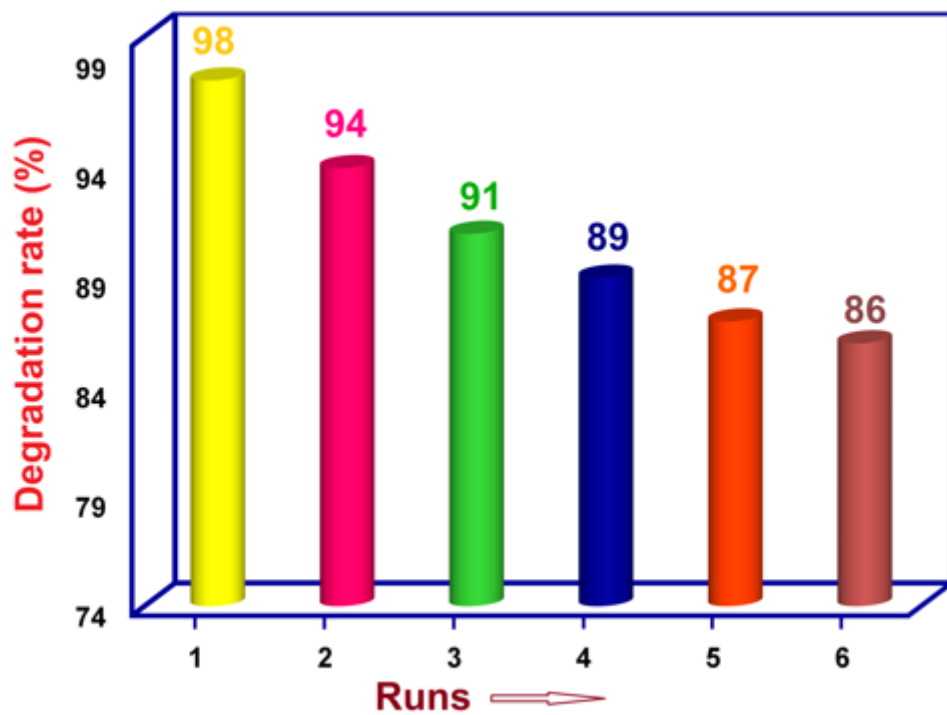


Figure 18

Recycled photo-catalytic activity testing of $\text{Cd}_{0.87}\text{Zn}_{0.1}\text{Cu}_{0.03}\text{S}$ for degradation of MB under UV irradiation for six cycles of degradation reaction.